UNIVERSIDADE FEDERAL DO RIO GRANDE DO SUL
INSTITUTO DE FÍSICA
PROGRAMA DE PÓS GRADUAÇÃO EM FÍSICA

Gustavo Ourique

Study of Cool White Dwarf Stars

Porto Alegre, Brasil
January 2, 2019

Gustavo Ourique

Study of Cool White Dwarf Stars

Dissertação submetida ao Programa de Pós-Graduação em Física do instituto de Física da UFRGS, como quesito parcial para obtenção do título de Mestre em Física, com ênfase em Astrofísica.

Supervisor: Alejandra D. Romero

Porto Alegre, Brasil

January 2, 2019

Gustavo Ourique

Study of Cool White Dwarf Stars

Dissertação submetida ao Programa de Pós-Graduação em Física do instituto de Física da UFRGS, como quesito parcial para obtenção do título de Mestre em Física, com ênfase em Astrofísica.

Trabalho aprovado. Porto Alegre, Brasil, *10* de *dezembro* de *2018*:

Alejandra D. Romero
Orientadora

Alan Alves Brito
Convidado 1

Antônio Kanaan
Convidado 2

Charles Bonatto
Convidado 3

Porto Alegre, Brasil
January 2, 2019

Acknowledgements

Agradeço a todos os professores que compartilharam comigo seu conhecimento ao longo dos anos da minha pesquisa. Agradeço especialmente a Profa. Dra. Alejandra Daniela Romero por todo auxílio e orientação durante meu mestrado e pelo tempo que pude passar com os quatro gatos que atualmente residem com ela, Copérnico, Fen, Galileo e Pandora, todos me ajudaram muito em minha pesquisa.

Agradeço ao Prof. Dr. Kepler de Souza Oliveira Filho por sempre me orientar e me ensinar a observar a ciência por trás dos dados que podem ser encontrados e como eles podem nos ajudar a compreender mais sobre o nosso universo. Agradeço a CAPES pelo financiamento da bolsa, essencial para que possamos produzir pesquisa de ponta. Agradeço aos meus colegas do grupo de pesquisa pelas reuniões semanais que, por mais que fossem um pouco extensas, sempre contribuíram ao conhecimento científico.

Também gostaria de agradecer aos meus pais pelo apoio e acolhimento nos momentos necessários da minha carreira. Agradeço aos meus avós, Olíria e Osvaldo Ourique, que sempre me apoiaram nos momentos mais difíceis da minha vida e sempre me mantiveram motivado para aprender coisas novas, tanto no trabalho quanto na vida.

Abstract

White dwarfs stars are the evolutionary endpoint for at least 97% of all stars in the Milky Way. Being the most common stellar fossil, they could be studied as a proxy for Galactic formation and evolution. White dwarfs also have information of the evolutionary path of their progenitors, which could be used to understand the physics of stellar evolution. The evolution of white dwarfs is practically a simple cooling, making them reliable cosmic clock to infer the age of stellar populations such as globular and open clusters and to the age of individual stars. The white dwarfs colder than 10 000 K provide us information of the oldest stars of the Milky Way. In this work, we calculated parameters such as photometric effective temperature, mass and distance for a sample of more than 20 000 spectroscopically confirmed white dwarfs. We present the mass distribution for DAs, DBs and DCs, the photometric effective temperature distribution for DAs, DBs, DCs, DZs and DQs and the distance distribution for DAs and non-DAs. We also present our calculation of the helium to hydrogen atmosphere white dwarf number ratio and compare with previous works. We discuss the consequence of a non-uniform distribution for this ratio, which lead us to information about the formation and evolutionary path of white dwarf stars.

Keywords: white dwarf; proper motion; photometry.

Resumo

Anãs brancas são o final da vida evolutiva de pelo menos 97% de todas as estrelas na Via Láctea. Sendo o fóssil estelar mais comum, elas podem ser estudadas como traçadores da formação e evolução da Galáxia. Anãs Brancas também possuem informação sobre caminho evolutivo de suas progenitoras, o que pode ser usado para compreender a física da evolução estelar. A evolução das anãs brancas é praticamente um simples resfriamento, fazendo delas relógios cósmicos confiáveis para se inferir a idade de populações estelares como aglomeradores abertos e globulares e da idade de estrelas individuais. As anãs brancas mais frias que 10 000 K nos fornecem informação sobre as estrelas mais velhas da Via Láctea. Neste trabalho, nós calculamos parâmetros como a temperatura efetiva fotométrica, massa e a distância para uma amostra com mais de 20 000 anãs brancas espectroscopicamente confirmadas. Nós apresentamos a distribuição de massa para as DAs, DBs e DCs, a distribuição de temperatura efetiva fotométrica para DAs, DBs, DCs, DZs e DQs e a distribuição de distância para as DAs e não-DAs. Nós também apresentamos o nosso cálculo da razão entre o número de anãs brancas com a atmosfera composta por hélio e o número de anãs brancas com a atmosfera composta por hidrogênio em função da temperatura efetiva e o comparamos com trabalhos publicados anteriormente. Nós discutimos sobre as consequências de uma distribuição não uniforme para essa razão, o que pode nos levar a informação sobre a formação e o caminho evolutivo das anãs brancas.

Palavras-chave: anãs brancas; movimento próprio; fotometria

List of Figures

List of symbols

DA	White dwarf with hydrogen lines on its spectrum.
DB	White dwarf with helium I lines on its spectrum.
DC	White dwarf without lines on its spectrum.
DO	White dwarf with helium II lines on its spectrum.
DQ	White dwarf with carbon lines on its spectrum.
DZ	White dwarf with metal lines on its spectrum.
Gy	Giga Year
K	Unit Kelvin
$M_{\odot}$	Solar Mass
T_{eff}	Effective Temperature
WD	White Dwarf

Contents

1 Introduction

1.1 Stellar formation and evolution

Stars are objects that remain stable for long timescales, which can last more than the age of the Universe and usually no less than some million years. The physical processes that lead to this stability are the equilibrium of all the forces involved in these objects interiors: gravity, pressure, magnetic field and rotation.

During the collapse of the molecular cloud due to the self-gravitation, a fraction of the energy will be lost and the remaining will heat up gas in the centre due to the virial theorem. If the cloud has more than 0.08 solar masses ($M_\odot$) it will heat up above to ~ 10 million of Kelvin, stable nuclear reactions will start in its centre, turning hydrogen into helium, providing a source of energy to counterbalance the gravitational collapse. It is defined as *Main Sequence* (MS) the stage where the star reaches the equilibrium of the gravitational force and the internal pressure. The MS is the longest evolutionary stage with nuclear reactions, which can last more than the current age of the universe if the initial stellar mass is below $\sim 0.45 M_\odot$. Objects that are born with less than $0.08\,M_\odot$ will never be able to ignite stable hydrogen nuclear fusion, leading to collapse until the object reaches the degenerate state to keep the equilibrium structure.

When the star runs out of hydrogen in the core, its core contract and the external layers expand, reducing the effective temperature and increasing the radius of the star to reach a new equilibrium state (Iben JR., 1965). This stage is called *Red Giant* (RG). In the RG, nuclear reactions of hydrogen are now in the layers around the helium core, increasing the core mass and temperature. At some point of its evolution, the star starts helium fusion in the core. The helium burning leads the star to a stage called *Horizontal Branch* (HB), where the luminosity is roughly stable and the effective temperature increases.

When the core runs out of helium, the star expands its external layers and reducing its effective temperature to reach a new equilibrium state. This stage is called *Asymptotic Giant Branch* (AGB). In this stage, helium is burned in the external shells of the core, increasing its mass until exhausts the helium in this region. During the AGB stage, the star loses most of its mass in form of strong winds.

For single star evolution, the final stage after the star life depends mainly on its initial mass. If the star was born with more than $\sim 11-11.8\,M_\odot$ (Smartt, 2009; Lauffer; Romero; Kepler, 2018) which according to the initial metallicity (Woosley; Heger, 2015; Romero; Campos; Kepler, 2015), the star will not be able to hold its own structure, collapsing and will end its life as a supernova. The remnant of this supernova will be a

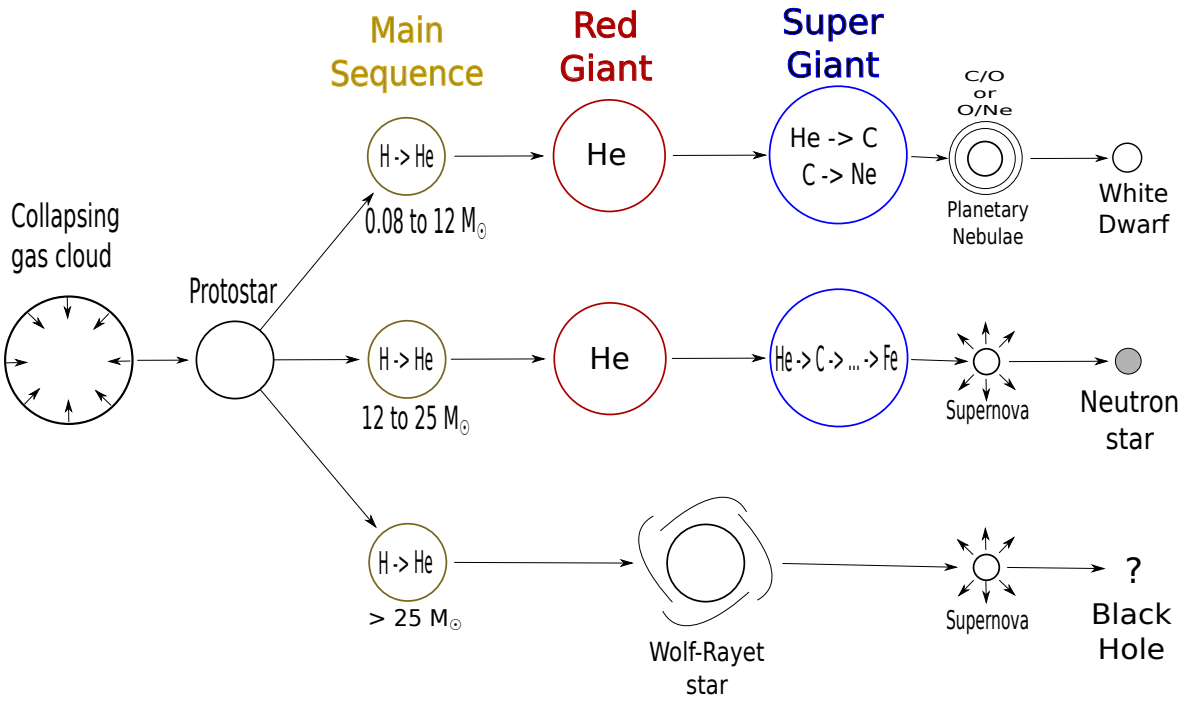

Figure 1 – Summary of the stellar evolutionary path according to the initial mass. If the star was born with more than $\sim 25\,M_\odot$ it will explode as a supernova and the remaining mass will be ejected during the explosion or will be turned into a stellar black hole. If the star was born with the mass between $\sim 12\,M_\odot$ and $\sim 25\,M_\odot$ it will explode as a supernova and the remaining will be a neutron star. If the star was born with the mass between $\sim 0.08\,M_\odot$ and $\sim 12\,M_\odot$ it will expel the external layers as a planetary nebula or burn all the remaining nuclear fuel, resulting in a WD. Below $\sim 0.08\,M_\odot$ the object will never be hot enough to burn the nuclear fuel to be considered as a star. Figure from Lauffer (2018).

neutron star if the initial mass is below $\sim 25\,M_\odot$ or a stellar black hole in the other case if the remaining mass was not ejected during the explosion.

Stars born with masses below $\sim 11-11.8\,M_\odot$ at the end of the thermal pulses could expel the external layers out as a planetary nebula. The result is a white dwarf, an exposed core composed of partially degenerated matter.

In Figure 1 we present a graphical summary of the evolutionary path according to the initial mass of the star.

1.2 White dwarf stars

White dwarf stars (WDs) are the evolutionary end-point for all stars that are born with masses from $0.08\,M_\odot$ to at least $\sim 11-11.8\,M_\odot$. These limits could vary according to

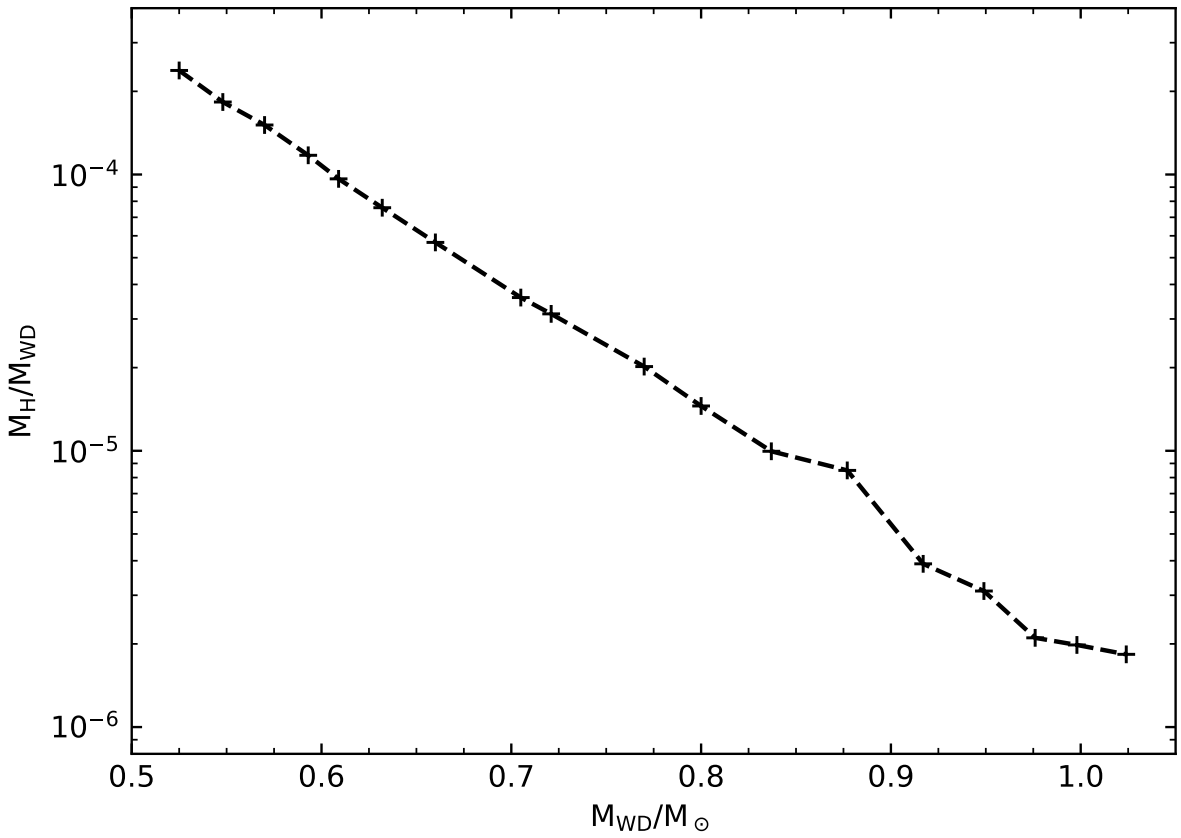

Figure 2 – Theoretical limit from Romero et al. (2012) models of the ratio between hydrogen layer mass and the total WD mass as a function of the total WD mass. Massive WDs present thinner hydrogen layers.

the stellar metallicity. The number of stars that are born in this mass interval corresponds to more than 97% of all stars (Winget; Kepler, 2008; Fontaine; Brassard, 2008; Althaus et al., 2010), making WDs the most common stellar fossils of the Milky Way.

Since the evolution of WDs is mostly a simple cooling, their age is well defined as a function of its mass and effective temperature, making them exceptional cosmic clocks and can be used to estimate the age of stellar populations such as globular and open clusters (Kalirai et al., 2001; Hansen et al., 2002; Hansen et al., 2007; Kalirai et al., 2013; Campos et al., 2016), or even the age of the Galactic disk, bulge and halo (Winget et al., 1987; Garcia-Berro et al., 1988b; Garcia-Berro et al., 1988a; Torres et al., 2002; Kilic et al., 2019).

The WD mass of the hydrogen envelope during its cooling depends on the total WD mass, being thinner for higher masses (Romero et al., 2012). In figure 2 we show the maximum hydrogen mass allowed by single stellar evolution computations as a function of the stellar mass.

After the WD is formed, it still has effective temperatures above 100 000 K, where

the cooling is mostly dominated by neutrino emission. While the WD cools down, the photon emission turns into the main cooling mechanism. At some point of the cooling, depending on the WD mass, the ion Coulomb energy exceed ∼220 times the thermal energy, crystallizing the WD core (Schneider et al., 2012) and releasing latent heat that warms it up (Winget et al., 2009), increasing the effective temperature and slowing its cooling for up to two gigayears. The effective temperature that defines when the WD will crystallize depends directly on the total mass of the WD, while WDs with masses higher than $1\,M_{\odot}$ crystallize at higher effective temperatures around ∼12 800 K, WDs with masses smaller than $0.52\,M_{\odot}$ crystallize at effective temperatures below ∼5 000 K.

WDs are classified according to their spectral features. The most common WDs spectroscopic class is known as DA and only presents hydrogen lines on their spectra. In panel "a" of Figure 3 we can see the optical spectrum of a typical DA. The spectral lines of WDs usually are wider than the lines of MS stars due to the high gravitational field. DAs corresponds to around 83% of the known sample of spectroscopically confirmed WDs published so far (Kleinman et al., 2004; Eisenstein et al., 2006; Kepler et al., 2015; Kepler et al., 2016).

The second most common spectroscopic class is known as DB and only present helium I lines. DBs corresponds to around 7% of the known sample of spectroscopic WDs. In panel "b" of Figure 3 we show the optical spectrum of a typical DB.

Following, we have DCs, that do not present any spectral line due to their low effective temperature and correspond to around 5% of the known spectroscopic WDs. In panel "c" of Figure 3 we show the optical spectrum of a typical DC. Is well known that DCs with effective temperature between ∼12 000 K and ∼5 000 K have an atmosphere composed of helium, since the presence of hydrogen would be evidenced by hydrogen lines in their spectra, while WDs with helium atmosphere only present spectral lines if the effective temperature is above ∼12 000 K. Below ∼5 000 K both hydrogen and helium atmosphere WDs do not present spectroscopic lines, not being possible to distinguish the composition of the WDs atmosphere via spectroscopy.

Around 4% of known spectroscopic WDs present metal lines from heavy elements like calcium and magnesium. The strong gravitational field of WDs drives heavy elements to their nucleus in less than 1 million years, very short timescales compared to its cooling timescale. So, spectral lines of heavy elements can only be seen in the WD spectrum if these elements are falling in the WD atmosphere on the last million years (Bergeron; Ruiz; Leggett, 1997; Bergeron; Leggett; Ruiz, 2001). Since these objects do not present hydrogen lines and their effective temperature is below ∼12 000 K, is known their atmosphere is composed of helium. In panel "d" of Figure 3 we can see the spectrum of typical DZ.

Around 1% of the known spectroscopic WDs present carbon lines or bands on its spectrum and are known as DQs. In panel "e" of Figure 3 we present the spectrum of

a hot DQ (effective temperature above 18 000 K), and a cool DQ (effective temperature below 10 000 K). The differences between the hot and the cool DQ spectrum is due to the carbon bands that only forms at cooler temperatures. The carbon in the WD atmosphere is probably a result of the dredge-up processes that drag the processed material from the WD interior to their atmosphere (Koester; Weidemann; Zeidler, 1982; Pelletier et al., 1986; MacDonald; Hernanz; Jose, 1998; Brassard et al., 2007; Dufour; Bergeron; Fontaine, 2005).

Less than 1% of the known spectroscopic WDs present helium II lines due to their higher effective temperature and are known as DO. In panel "f" of Figure 3 we can see a spectrum of a typical DO.

Some other classes are known, such as DS (Kepler; Koester; Ourique, 2016), WDs with the spectra dominated by oxygen lines, but they are not statistically significant yet to include on this study.

Mixed spectroscopic classes, such as DABs and DBAs, WDs that present both hydrogen and helium lines on their spectra, can also be found in our catalogues. Due to the unreliability in the photometric parameter estimation, we do not include a direct analysis of these objects in this work.

1.3 Motivation

Nowadays, the cooling process of WDs is well known (Mestel, 1952; van Horn, 1967). However, the formation of WDs of specific atmosphere composition is not completely understood yet.

The most common WD formation scenario asserts that at some point of the evolution of the star after the giant stage, the star will eject its external layers. The remnant will be an exposed nucleus, it furthermore called as WD. In this scenario, the WD will have hydrogen on its atmosphere and later its spectrum will only present hydrogen lines, being classified as DA.

An alternative path is associated with the presence of a very late thermal pulse in the evolution (Fujimoto, 1977; Schoenberner, 1979; Iben JR., 1984; Iben JR.; MacDonald, 1995). After the thermal pulse stage and the planetary nebula stage, the star is entering the WD cooling sequence. However, it could perform a very late thermal pulse by igniting the helium. Due to the energy generated by the helium burning, all the remaining hydrogen is burned, resulting in a pure helium atmosphere WD

The very late thermal pulse scenario offers a path for the formation of the helium atmosphere WDs. However, the fraction of helium atmosphere WDs at effective temperatures above 20 000 K is around 7%, but this fraction increases to around 30% for effective temperatures below 10 000 K. Theory suggests the very late thermal pulse is a rare event,

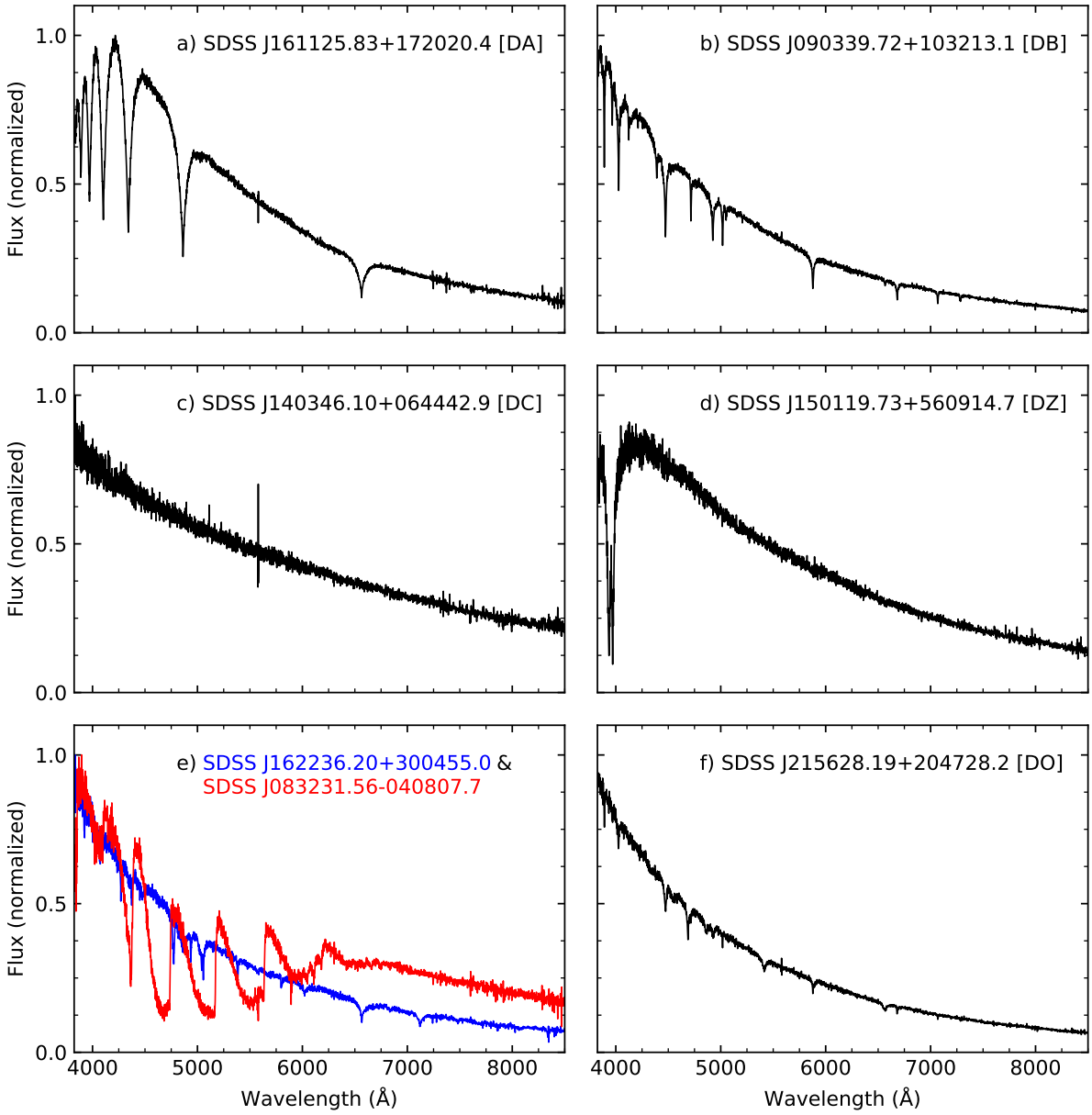

Figure 3 – Spectra of typic WDs of different spectral classes. In panel "a", "b", "c", "d" and "f" we have the spectra of the WDs, respectively, *SDSS J161125.83+172020.4* (DA), *SDSS J090339.72+103213.1* (DB), *SDSS J140346.10+064442.9* (DC), *SDSS J150119.73+560914.7* (DZ) and *SDSS J215628.19+204728.2* (DO). In the panel "e" we have the spetrum of the hot DQ *SDSS J162236.20+300455.0* (blue line) and the cool DQ *SDSS J083231.56-040807.7* (red line). All these spectra were obtained from the SDSS spectroscopic database and the flux maximum value are normalized to 1.

not happening to more than 10% of all the WDs (Althaus et al., 2005). This implies that, either the theory of very late thermal pulse is wrong, or we have an alternative path that enhances the formation of helium atmosphere WDs.

In this work, I verify the viability of alternative paths for the formation of helium atmosphere WDs without the strict dependence of the very late thermal pulse. I focus on three alternative paths: Peculiar stellar population, different cooling rates from helium and hydrogen atmosphere WDs and convective dilution and mixing, i.e., spectral evolution.

1. The peculiar stellar population hypothesis assumes that the formation of helium atmosphere WDs depends on a stellar parameter, such as metallicity, mass loss or overshooting, leading to the formation of an H-deficient remnant.

2. The second hypothesis is that hydrogen and helium atmosphere WDs have different cooling rates. It is well known that helium atmosphere WDs cool faster than hydrogen ones until reach 5 000 K due to the lower opacities (Bergeron; Leggett; Ruiz, 2001). Even if the number of helium atmosphere WDs formed by the very late thermal pulse is around 10%, if they cool down significantly faster than hydrogen atmosphere WDs we should find more helium atmosphere WDs at lower temperatures, being possible to measure a higher ratio.

3. The last hypothesis that will be discussed in this work is the convective mixing and dilution (Shipman, 1989; Fontaine; Wesemael, 1987; Bergeron et al., 1990). Rolland, Bergeron e Fontaine (2018), for example, discussed the evolution of the hydrogen atmosphere WDs, where at some point of the WD cooling sequence the hydrogen could be diluted or mixed with the helium layer, turning it on a helium atmosphere WD. The convective dilution event occurs for effective temperatures around 20 000 K and no more than 32 000, K, while the convective mixing occurs for effective temperatures below 12 000, K, according to Rolland, Bergeron e Fontaine (2018). These convective events can increase the number of helium atmosphere WD for lower effective temperatures.

2 Method

2.1 Data Sample

Since this work study the formation and evolution scenario for helium and hydrogen atmosphere WDs, it is necessary to have a large data sample of spectroscopically classified WDs to avoid small data sample bias.

Our initial sample is composed of all WDs classified as DA, DB, DC, DZ or DQ in the SDSS spectroscopic WD catalogue (Kleinman et al., 2004; Eisenstein et al., 2006; Kepler et al., 2015; Kepler et al., 2016) in addition to all WD candidates from Munn et al. (2014) deep proper motion catalogue (Munn et al., 2017), that are spectroscopically confirmed as WD and classified in this work. Furthermore, we decided to include only objects with parallaxes determined by *Gaia Survey* to ensure the trustworthiness of our further determinations. The resulting data sample is composed of 17 492 DAs, 1 766 DBs, 1 290 DCs, 557 DZs and 279 DQs, totaling 21 384 WDs.

For all objects in the initial data sample we have magnitudes for each SDSS filter, u, g, r, i, z and their respective uncertainties, the reddening, A_V and the *Gaia* parallaxes and parallaxes uncertainties. Furthermore, all magnitudes used in this work are fully de-reddened using Schlegel, Finkbeiner e Davis (1998) reddening maps and Yuan, Liu e Xiang (2013) extinction coefficients and ignoring the influence of distance on the reddening.

2.2 Parameter Determination

Owing to the different catalogue origin for several objects in our data sample, the fitting parameters from literature do not follow a uniform determination method. To avoid bias coming from different fitting routines, we developed a fitting routine to be applied to all objects of our sample that only depends on the photometry and the parallax.

For a set of parameters and the respective uncertainties, we resample each input parameter according to its uncertainty following an assumed distribution. For each set of resampled parameters, we calculate the solution function that provides us with the output parameters of interest. From that, for each output parameter, we have a solution distribution. The median of each solution distribution will be assumed as the general solution, the difference between the median and the 16 percentile as the lower uncertainty and the difference between the 84 percentile and the median as the upper uncertainty.

In this work, we assume a normal distribution for the input parameters with the median as the observed value and width as the observed uncertainty. Also, we assume

as the solution function the least squares (Legendre; Gauss; Laplace, 1806,1809,1810) of input parameters with the parameters provided by a set of models. These models will be better explained in section 2.3.

In figure 4 we can see an example the method used in this work for a unidimensional input parameter resulting in one parameter solution.

2.3 Models

To determine parameters such as effective temperature, $\log g$, mass and distance, we applied the method described in section 2.2, comparing for each object the de-reddened colours to a synthetic colour grid provided by Koester (2010), Koester e Kepler (2015) and Carrasco et al. (2014) models, that associates these parameters with photometric synthetic colours. As we have the parallaxes, we can use the object distance to limit the colour grid according to the object total luminosity. For that, we include Carrasco et al. (2014) luminosity models associated with the object parameters such as effective temperature, mass and absolute magnitude.

For DAs, we used hydrogen-rich atmosphere WD synthetic colour models, while for DBs and DCs we used pure helium-rich atmosphere WD synthetic colours. For both, we can recover parameters such as effective temperature, mass and distance. For DQs and DZs we used, respectively, carbon-rich and metal-rich atmosphere WD synthetic colour models. However, for DQs and DZs we can only recover the effective temperature and distance since the colours provide degenerate solutions on the mass and carbon or metal abundances in the atmosphere.

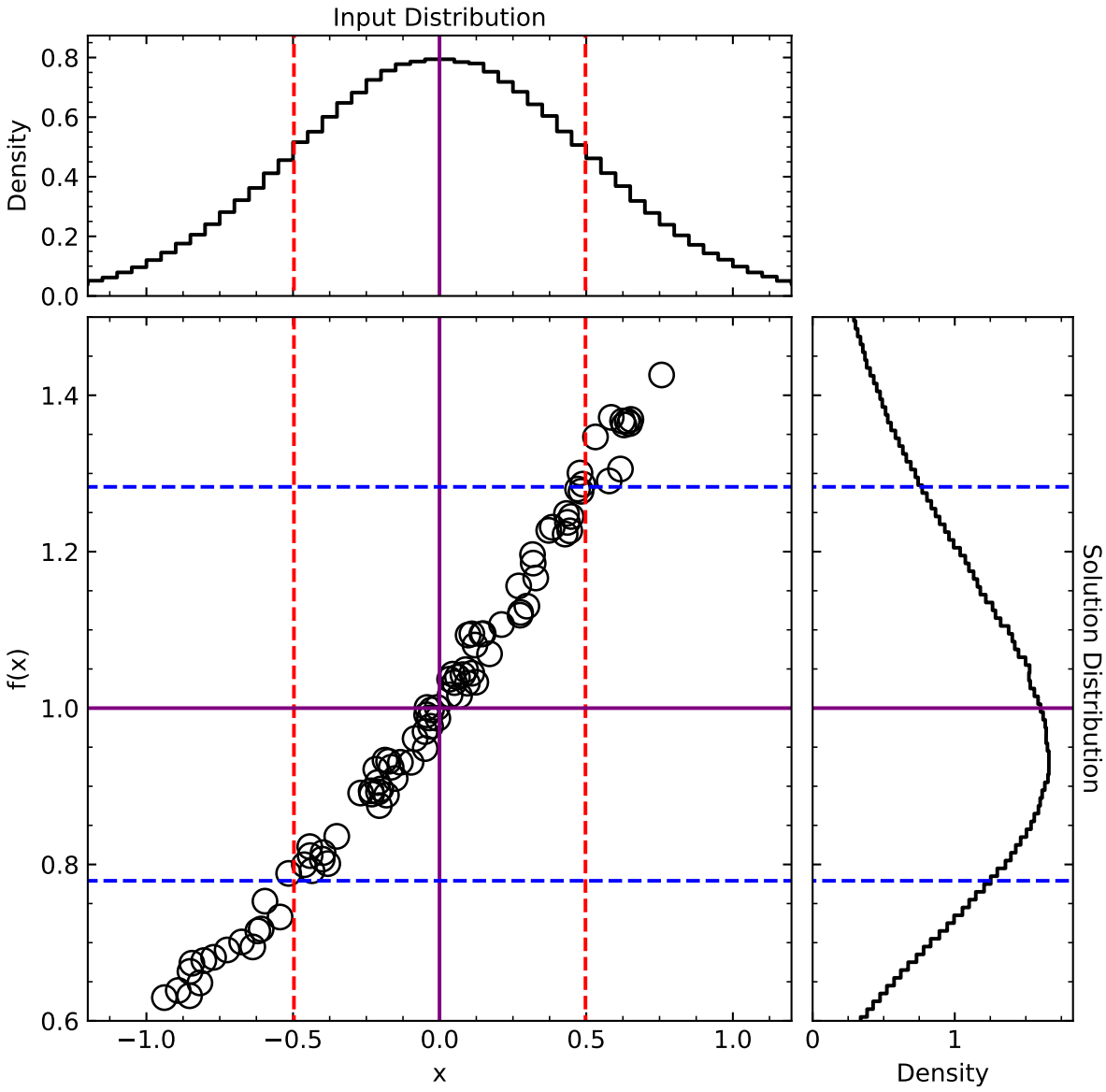

Figure 4 – Graphical description of the Monte Carlo procedure to parameter estimation applied to one-dimensional data and its respective uncertainty. The middle panel is the input data and the calculated solution function. The top panel presents the input parameter distribution, while the right panel presents the solution parameter distribution. The red dashed lines indicate the 16 and 84 percentiles in the input parameter distribution. The blue dashed lines indicate the 16 and 84 percentiles in the solution parameter distribution. The purple solid lines indicate the median of the input and solution distribution. Given an input parameter and its respective uncertainty, it was resampled assuming a distribution. In this case, the normal distribution was assumed. For each resampled point we calculated the solution function, providing a solution distribution where the median is assumed as the general solution and the difference between the median and the percentiles 16 and 84 provides the lower and upper uncertainty respectively.

3 Results

3.1 Masses

Since most used methods to estimate masses for WDs are dependent on the spectroscopic lines, there is no mass distribution for DCs in the literature. Due to the degenerated matter that composes most of the WD mass, its mass follows a direct relation with its radius, known as *mass-radius relation* (Romero; Campos; Kepler, 2015; Cummings et al., 2018). The determination of the WD distance and luminosity together with the measure of its flux gives us a direct relationship with its radius, that, together with the *mass-radius relation* could be used to estimate the WD mass.

As a result of the method described in section 2.2 applied to our data, we have estimated masses for all DAs, DBs and DCs of our sample. In Figure 5 we present the mass distribution for DAs, DBs and DCs. We can notice that DA and DB distributions have the same mode at $0.55\,M_{\odot}$ and nearly the same shape. The main difference between DA and DB distributions is that DAs present excess at lower and higher masses. The most probable cause of these excesses comes from interacting binary evolution. For interacting binaries, two common scenarios are increasing the total mass of one of them by mergers or decreasing the total mass by mass loss. Both scenarios could happen to WDs, and in both cases it is very probable that the WD will accrete some hydrogen, turning any DB in an interacting binary system into a DA. We also can notice that DCs are significantly more massive than DAs and DBs, with a mode around $0.75\,M_{\odot}$. The dashed region indicates all objects with masses below $0.45\,M_{\odot}$. This region is dashed to emphasize the fact that any star below this mass could not be turned into a WD by single star evolution in timescales shorter than the age of the Universe (Liebert; Bergeron; Holberg, 2005; Rebassa-Mansergas et al., 2011).

To avoid objects that came from binary evolution in our further analysis, we remove from our sample all objects with an estimated mass below $0.45\,M_{\odot}$, reducing our sample of DAs, DBs and DCs to 13 678, 1 428 and 1 173 objects, respectively.

3.2 Photometric Effective Temperature

We determine the photometric effective temperature for all objects in our sample. Considering that the spectroscopic effective temperature found in each catalogue is determined with a different model grid and fitting technique, we test if our determinations on average agree with the determinations from the literature. In Figure 6 we show the

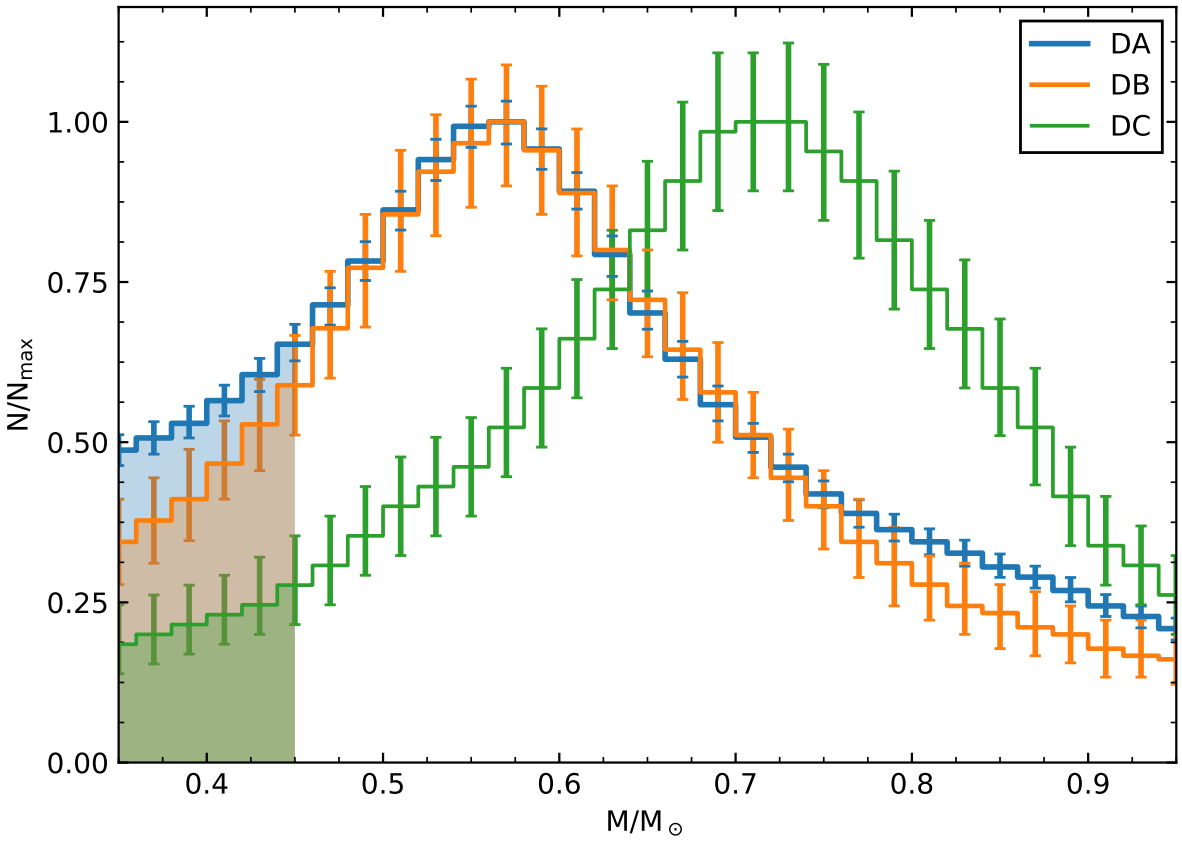

Figure 5 – Mass distribution for DAs, DBs and DCs. The distribution uncertainties are calculated by resampling the data over their uncertainty. We can notice that DAs and DBs have nearly the same distribution by both having a peak around $0.55\,M_\odot$ and a similar shape, except for an excess in higher and lower masses in the DAs distribution. The DCs distribution is significantly more massive than DAs and DBs distribution, with a peak around $0.75\,M_\odot$. Objects with masses below $0.45\,M_\odot$ would take more than the age of the Universe to turn into WD by single star evolution, so the shaded region indicates objects that originated from interacting binaries. All distributions are normalized by their maxima.

comparison of the photometric effective temperature determined in this work and the spectroscopic effective temperature provided by the catalogues. Our determinations are 7% cooler on average, which could be a consequence of the full de-reddening applied.

For each spectroscopic class in our sample, we calculated the effective temperature distribution, shown in Figure 7. In this figure, we can notice that DBs can only be found at effective temperatures higher than 12 000 K, which is expected since WDs below this effective temperature cannot present helium lines, at least with signal-to-noise below 60 in spectra obtained by SDSS, indicating that these DBs already have turned into DCs. We can see in the figure that DC, DQ and DZ have nearly the same distributions, with objects with effective temperatures below 12 000 K. Unlike the other distributions, the DA distribution is much wider, having significant counts at higher and lower effective

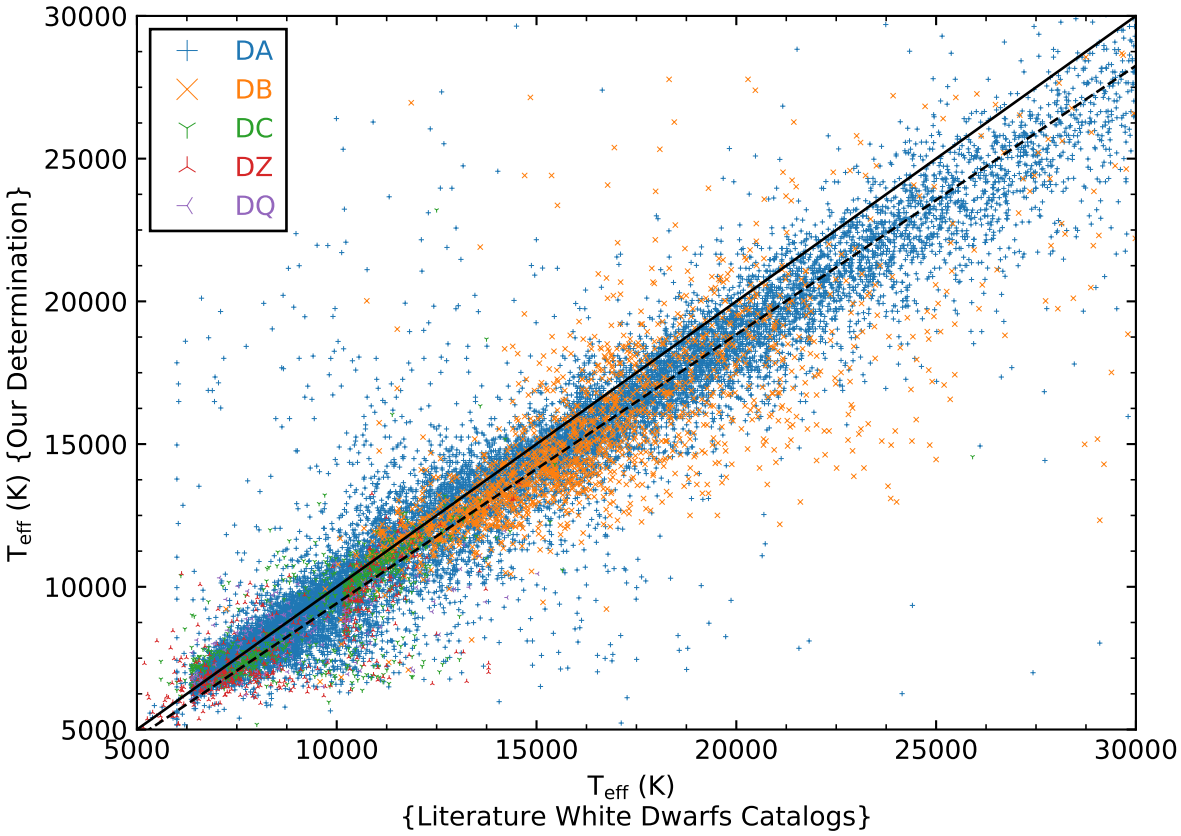

Figure 6 – Comparison of the photometric effective temperature determined on this work and the spectroscopic effective temperature provided by the catalogues. The solid black line represents the identity and the dashed black line represents the linear fit indicating that our determinations are 7% cooler on average.

temperatures.

In Chapter 1 we described that the most probable origin of DCs, DQs and DZs are by some evolutionary process that happens on helium-rich atmosphere WDs. Thus, we group all objects of our sample that come from the evolution of helium-rich atmosphere WDs in one class, that we call as *non-DA*. This assumption is very convenient to compare the formation and evolution channels of helium-rich and hydrogen-rich atmosphere WDs, as our sample does not extend below 5 000 K, where DAs also turn into DCs. In Figure 8 we show the effective temperature distribution for DAs and non-DAs. In this figure, we can notice that DA distribution increases in number counts from 30 000 K to ∼7 000 K and present a local minimum around 12 000 K. On the other hand, the non-DA distribution only presents the increases in counts from 30 000 K to 7 000 K.

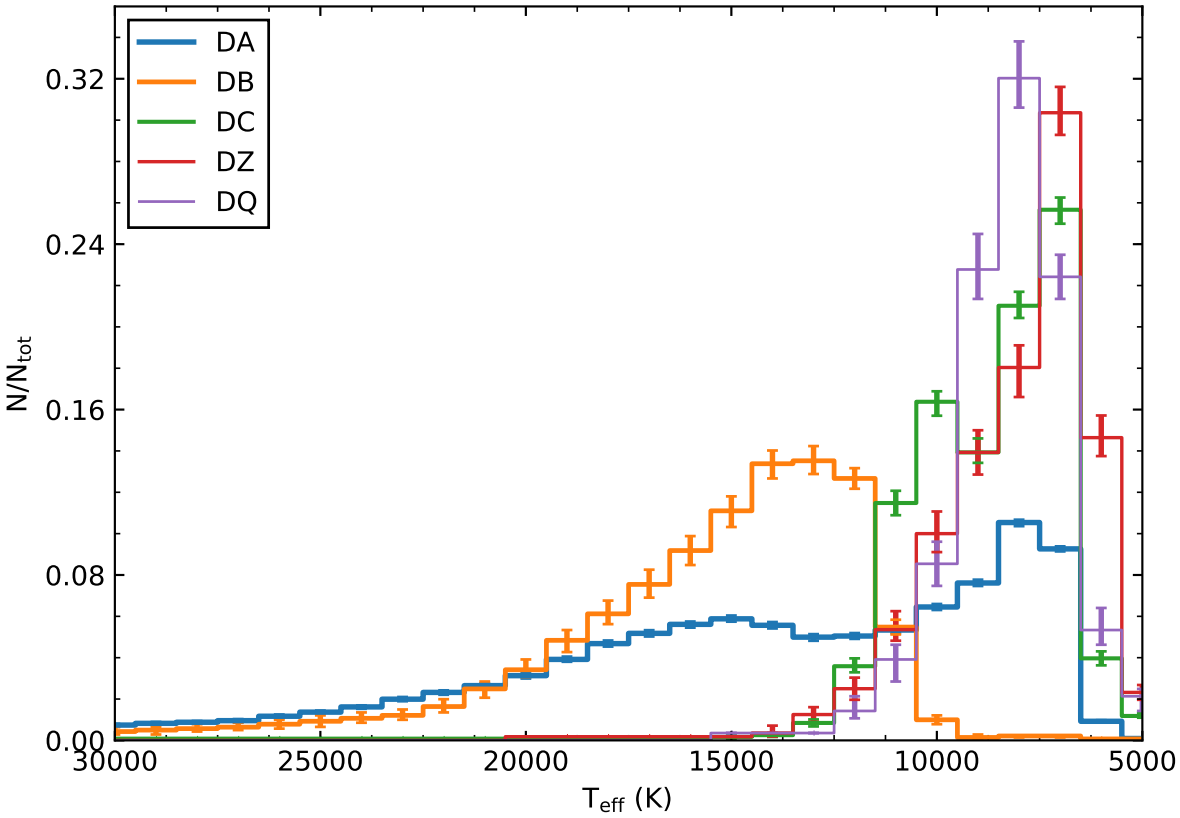

Figure 7 – Photometric effective temperature distribution for DAs, DBs, DCs, DQs and DZs. The DA distribution (blue) has significant counts at all effective temperatures of our study. The DB distribution only present significant counts for effective temperatures above 12 000 K, while DC, DQ and DZ distributions only present significant counts below 12 000 K. All distributions are normalized by their total counts.

3.3 Distance

The distance distribution of DAs and non-DAs can be seen in Figure 9. We can see in the figure that the DA distribution is very extended to higher distances and present a possible bimodality around 250 pc. However, due to the low statistical significance of this bimodality, we will not discuss this feature.

3.4 Completeness

We can notice from Figure 9 that DAs and non-DAs do not have the same distance distribution. This characteristic could create a bias in our analysis when we try to compare them. To avoid this possible bias, we select a sub-sample composed by all objects with the magnitude on filter g higher than 14.5 and smaller than 19.0, i.e., 5 336 DAs and 1 315 non-DAs, and weighted each object on the distributions according to the inverse of

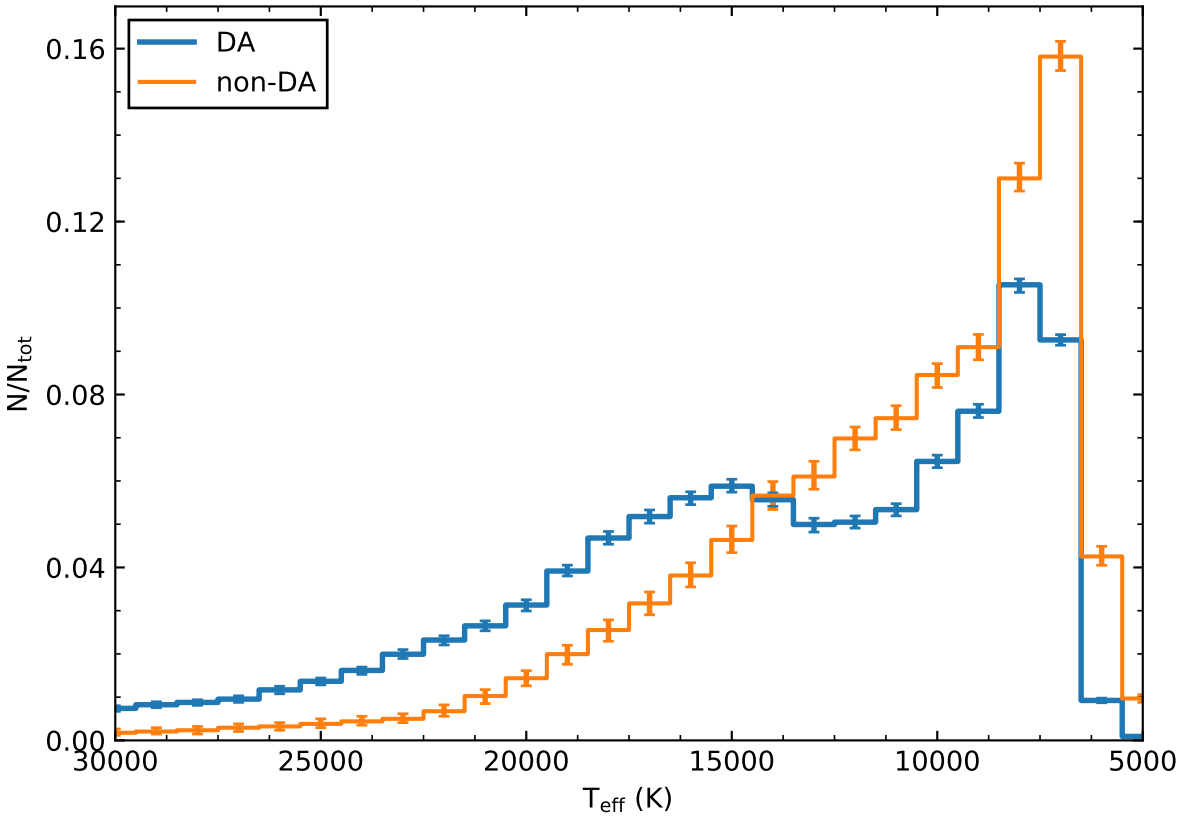

Figure 8 – Photometric effective temperature distributions for DAs and non-DAs. We can see that both distributions present a peak around 7 000 K. A bimodality can be seen in the DA distribution, showing a second peak around 16 000 K. Both distributions are normalized by the total number of counts.

the observed volume that these objects occupy assuming an old star galactic disk scale height of 300 pc (Schmidt, 1968; Schmidt, 1975; Green, 1980; Stobie; Ishida; Peacock, 1989; Liebert; Bergeron; Holberg, 2003; Kepler et al., 2007; Limoges; Bergeron, 2010; Rebassa-Mansergas et al., 2015, for more details).

On Figure 10 we have the mass distribution for DAs, DBs, DCs and the sum of these three distributions. We can see that DBs are less significative than DCs for the entire distribution. Also, we can notice that the density excess at masses below 0.45 $M_\odot$ is mostly a DA contribution. The excess of massive DAs probably comes from mergers.

On Figure 11 we show the volume corrected distribution of effective temperature for DAs and non-DAs. It is possible to notice that the distributions are very similar, where the largest difference is the higher density of DAs at effective temperatures above 12 000 K. The density decrement near 5 000 K occurring for both distributions is an evidence that they have the same maximum age.

On Figure 12 we show the volume corrected distance distribution for DAs and non-DAs. Both distributions have the same shape, being a strong evidence that both

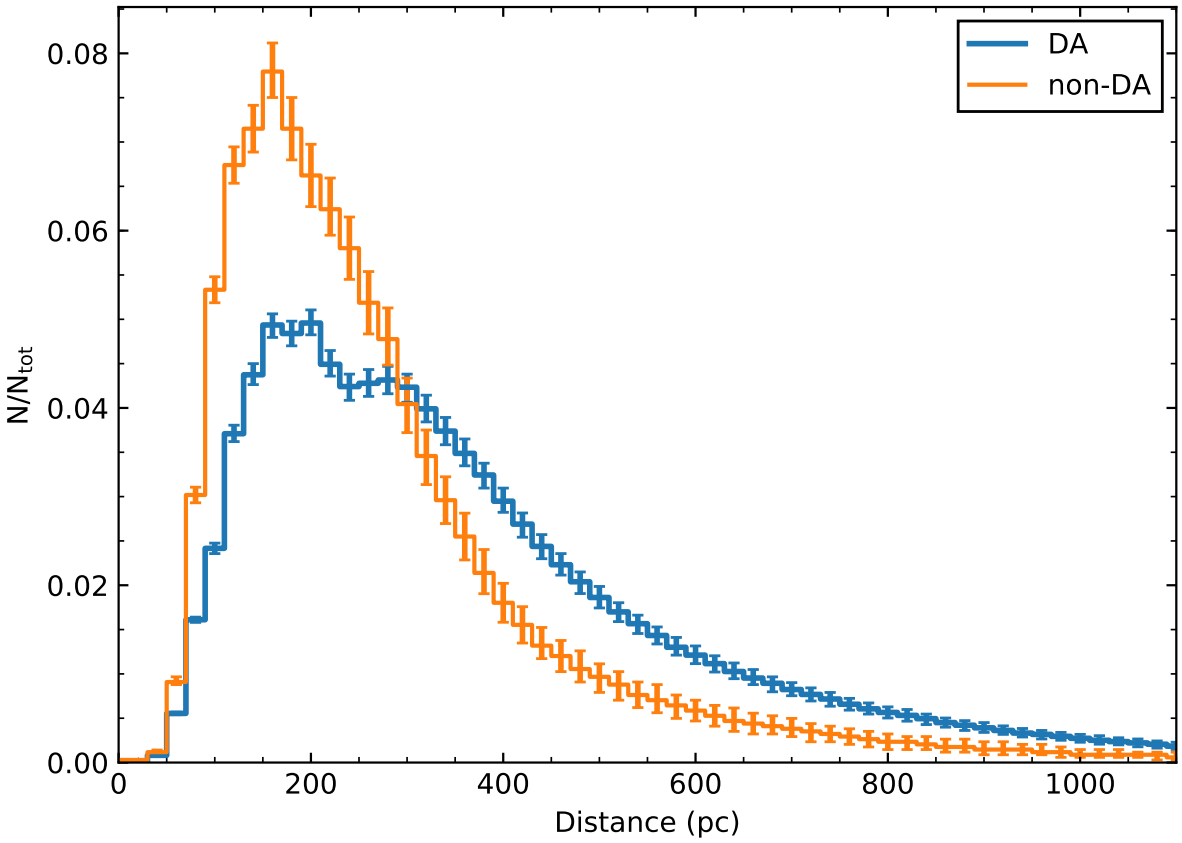

Figure 9 – Distance distributions for DAs and non-DAs. Both distributions present a peak around 200 pc. The DA distribution has significantly more counts at higher distances than the non-DA distribution. It is possible to notice a bimodality on the DA distribution, but due to the low statistical significance, we will not investigate its origin. Both distributions are normalized by the total number of counts.

samples follow the same spatial completeness.

3.5 Helium to Hydrogen Atmosphere WD Number and Density Ratio

One way to study where the evolution and formation of DAs and non-DAs differs is calculating the ratio between properties of both samples. Tremblay e Bergeron (2008) presented in their work the ratio between the number of helium atmosphere and hydrogen atmosphere WDs as a function of the effective temperature for a sample of less than 500 objects. One of the results of Tremblay e Bergeron (2008) study is that this ratio increases for effective temperatures lower than 10 000 K. They proposed that this increase is a consequence of the convective mixing, turning some 15% of hydrogen atmosphere WDs into helium atmosphere WDs.

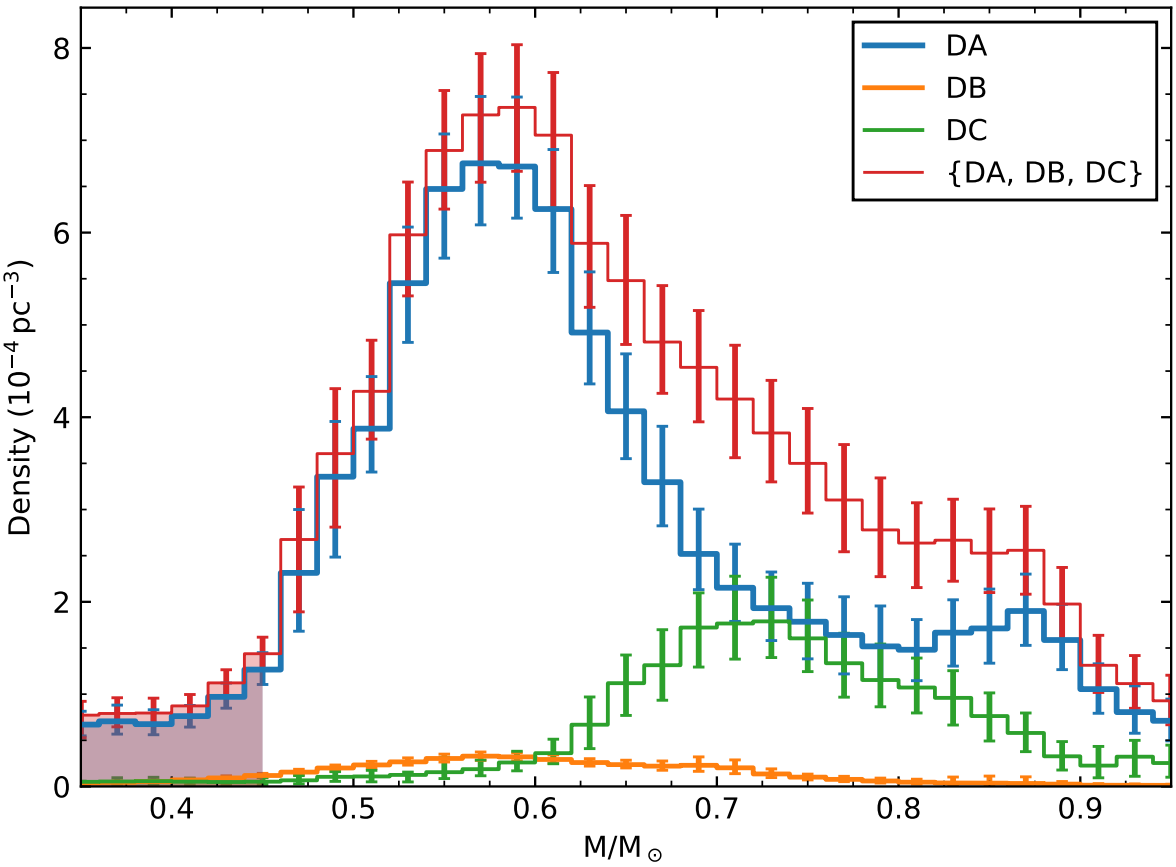

Figure 10 – Effective temperature distribution corrected by volume for DAs, DBs, DCs and the sum of the three samples. We can notice an excess of DAs at masses below 0.45 $M_\odot$ and above 0.8 $M_\odot$, objects that probably come from binary evolution. Due to its higher luminosities, DBs are not significant for the total density of WDs. The high density of massive DCs affects directly the total mass distribution.

On Figure 13 we have our estimative of the helium to hydrogen atmosphere WD number ratio for our main sample (blue) and density ratio for our volume corrected sample (orange). We also present on this plot the ratio calculated by Tremblay e Bergeron (2008). In this figure, we can notice that the range in effective temperature of our study extends to higher values than the one studied by Tremblay e Bergeron (2008), varying from 30 000 K to 5 000 K. Our sample presents an increase in the slope of the helium to hydrogen atmosphere WD number and density ratio from around 22 000 K, followed by a second increase around 14 000 K and do not present the same increase below 10 000 K that Tremblay e Bergeron (2008) described in their determination. Since WDs below 5 000 K do not present hydrogen lines, we can not distinguish DAs and non-DAs closer to 5 000 K, making any measure not reliable in this region.

Rolland, Bergeron e Fontaine (2018) discussed that events of convective dilution occur at effective temperatures between 32 000 K and 20 000 K if the hydrogen layer is

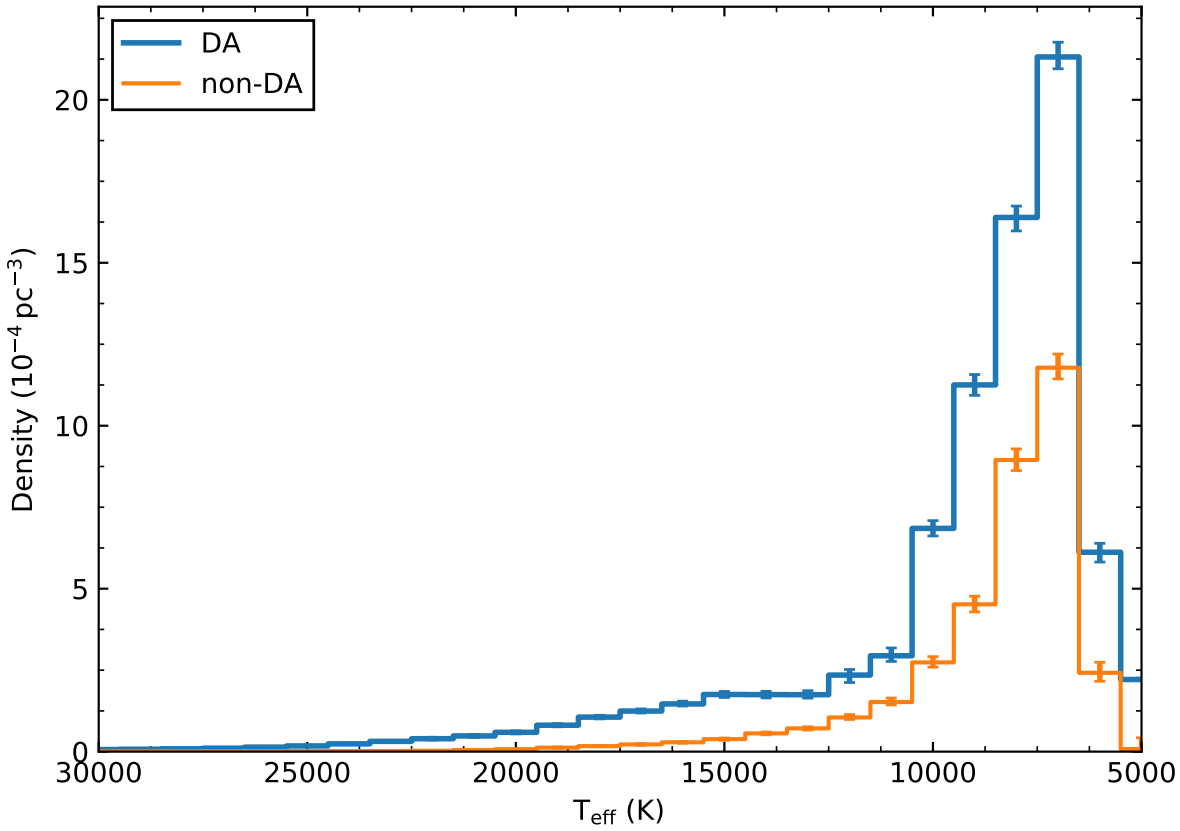

Figure 11 – Effective temperature distribution corrected by volume for DAs and non-DAs. Is possible to notice that both distributions are very similar, except for the excess of DAs with effective temperature above 12 000 K.

thin, with $M_H/M_\odot \lesssim 10^{-12}$. This event could turn DAs into non-DAs. Rolland, Bergeron e Fontaine (2018) also discussed that convective mixing could turn DAs into non-DAs at effective temperatures around 12 000 K. These two convective events match with the changes of slope observed on our determination of helium to hydrogen atmosphere WD number ratio. Also, Kepler et al. (2016), Kepler et al. (2015), Eisenstein et al. (2006), Kleinman et al. (2004) reported around 250 DABs at 24 000 K and around 150 DBAs at 13 000 K. The main spectral properties of DBAs and DABs is that they present both hydrogen and helium lines. This is a possible evidence that these objects are transitioning objects due to convective processes.

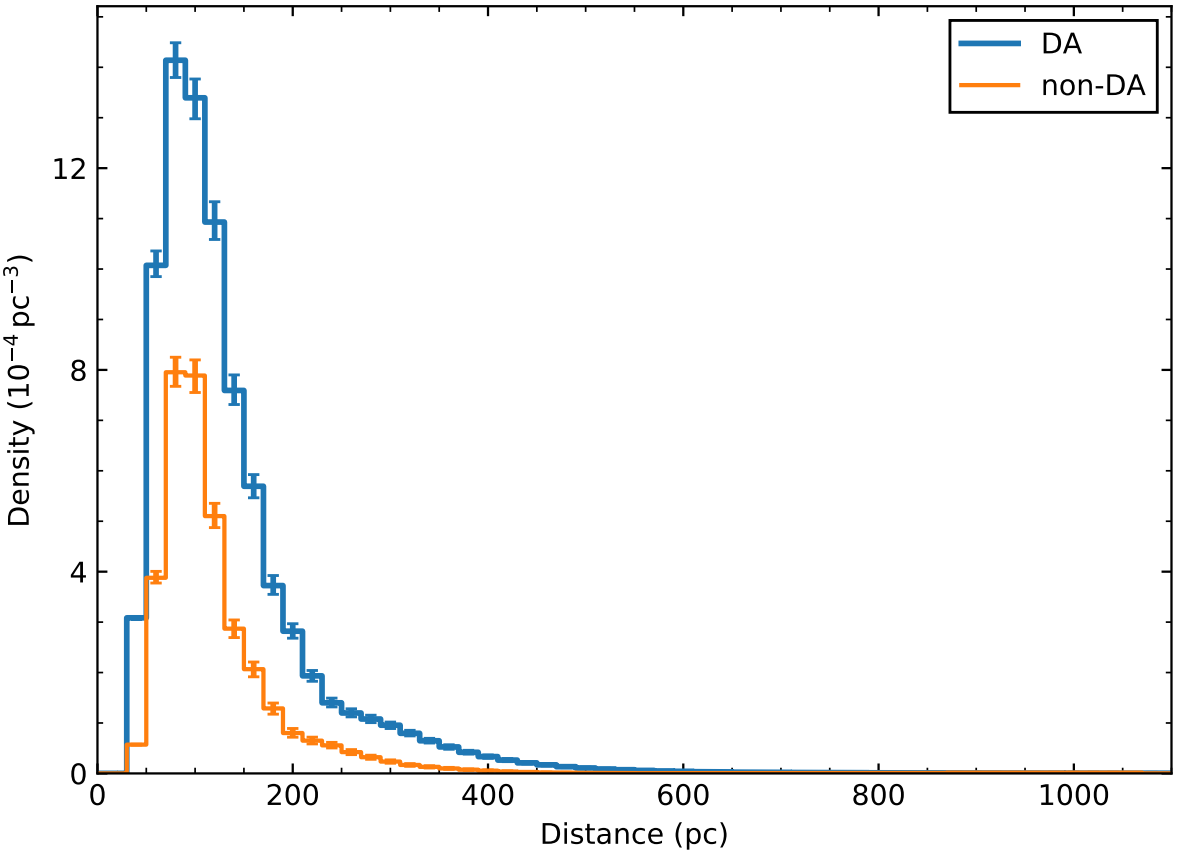

Figure 12 – Distance distribution correct by volume for DAs and non-DAs. The similar shape for both distributions is an evidence that they have the same completeness.

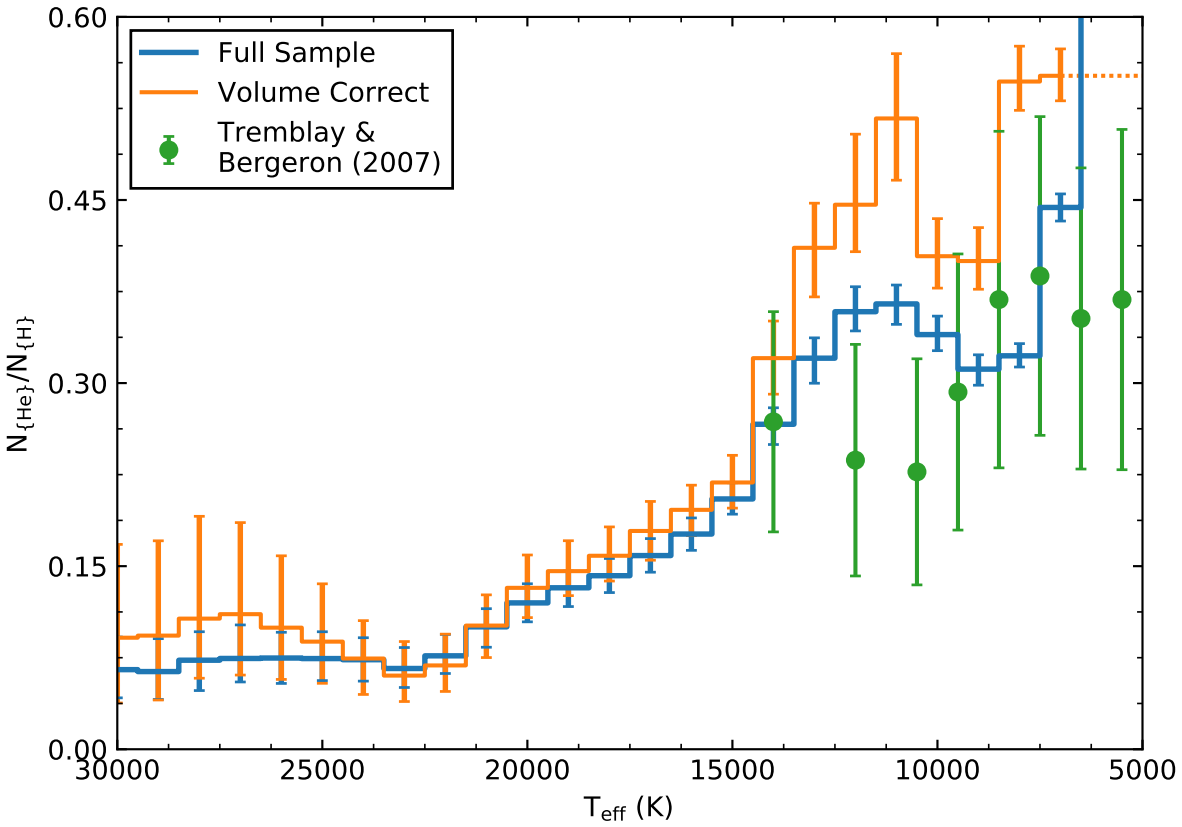

Figure 13 – Helium to hydrogen atmosphere WD number and density ratio. Our determinations show that the ratio increases from ∼0.075 at 22 000 K to ∼ 0.36 at 12 000 K. Tremblay e Bergeron (2008) determination do not present any increase from 15 000 K to 12 000 K and present an increase around 10 000 K that can not be seen on our determinations. The low impact of the volume correction implies that DAs and non-DAs sample have nearly the same completeness.

4 Conclusion

In this work, we find that DAs and DBs have nearly the same mass distribution, both with the mode around $0.55\,M_\odot$. The main difference between the DA and DB mass distribution is an excess of counts of DAs at masses below $0.45\,M_\odot$ and above $0.85\,M_\odot$. Since any WD with a mass below $0.45\,M_\odot$ could not be formed in the age of the Universe by single star evolution, these objects should be formed by binary evolution. The massive excess could be explained by a merger population that increases the total mass of the WD. We also found that the DCs are significantly more massive than DAs and DBs, having a mode around $0.7\,M_\odot$.

We do not find the same increase in the helium to hydrogen atmosphere WD number ratio for effective temperatures below 10 000 K presented by Tremblay e Bergeron (2008). We assume that their small sample misleads their conclusion since the increase observed in their determinations have nearly the same amplitude as their uncertainty.

We determine that our helium to hydrogen atmosphere WD number ratio increases from ∼0.075 to ∼0.36 at effective temperatures from 22 000 K to 12 000 K. The main hypotheses that are proposed to explain this increase are a peculiar population, different cooling rates of DA and non-DAs and convective mixing and dilution.

One of the best evidences that could indicate the existence of a peculiar population is that the two populations have different spatial distributions. In Figure 12 we can notice that the two spatial distributions are very similar, only varying in the total density. A second evidence is that the two populations should not have the age. To reproduce our data we would need a DA population with a continuous formation and a non-DA population only with stars younger than 0.75 Gyr. This much younger population is very improbable in a Galactic evolution scenario and Figure 11 indicates that both populations have the same maximum age. We, therefore, do not consider the peculiar population as a viable explanation of the helium to hydrogen atmosphere WD number ratio.

It is well known that DA and non-DAs have different cooling rates (Bergeron; Leggett; Ruiz, 2001). In this work, we verified that the cooling rates difference from Romero, Campos e Kepler (2015) and Tremblay, Bergeron e Gianninas (2011), Bergeron et al. (2011) models cannot reproduce the helium to hydrogen atmosphere WD number ratio.

Spectral evolution by convective mixing and dilution is a consistent solution for the increase of the helium to hydrogen atmosphere ratio since we found two changes in the slope of the ratio in the same effective temperature range of convective events. Furthermore, convective mixing and dilution are more probable to occur on massive DAs since they

have thinner hydrogen layers (Romero et al., 2012). Our calculated DC mass distribution indicates that most non-DAs are more massive than DAs, which can be an evidence that massive DAs performed the convective mixing or dilution during their evolution.

In our future work, we will study the consequence of the convective mixing and dilution in the colour-magnitude diagram for a synthetical WD population, and then compare the synthetical population with the WD population of big surveys, such as SDSS and *Gaia*.

Bibliography

Althaus, L. G. et al. Evolutionary and pulsational properties of white dwarf stars. *A&ARv*, v. 18, p. 471–566, out. 2010. Citado na página 21.

Althaus, L. G. et al. The formation and evolution of hydrogen-deficient post-AGB white dwarfs: The emerging chemical profile and the expectations for the PG 1159-DB-DQ evolutionary connection. *A&A*, v. 435, p. 631–648, maio 2005. Citado na página 23.

Bergeron, P.; Leggett, S. K.; Ruiz, M. T. Photometric and Spectroscopic Analysis of Cool White Dwarfs with Trigonometric Parallax Measurements. *ApJS*, v. 133, p. 413–449, abr. 2001. Citado 3 vezes nas páginas 22, 25, and 41.

Bergeron, P.; Ruiz, M. T.; Leggett, S. K. The Chemical Evolution of Cool White Dwarfs and the Age of the Local Galactic Disk. *ApJS*, v. 108, p. 339–387, jan. 1997. Citado na página 22.

Bergeron, P. et al. A Comprehensive Spectroscopic Analysis of DB White Dwarfs. *ApJ*, v. 737, p. 28, ago. 2011. Citado na página 41.

Bergeron, P. et al. On the surface composition of cool, hydrogen-line white dwarfs - Discovery of helium in the atmospheres of cool DA stars and evidence for convective mixing. *ApJ*, v. 351, p. L21–L24, mar. 1990. Citado na página 25.

Brassard, P. et al. The Origin and Evolution of DQ White Dwarfs: The Carbon Pollution Problem Revisited. In: Napiwotzki, R.; Burleigh, M. R. (Ed.). *15th European Workshop on White Dwarfs*. [S.l.: s.n.], 2007. (Astronomical Society of the Pacific Conference Series, v. 372), p. 19. Citado na página 22.

Campos, F. et al. A comparative analysis of the observed white dwarf cooling sequence from globular clusters. *MNRAS*, v. 456, p. 3729–3742, mar. 2016. Citado na página 21.

Carrasco, J. M. et al. Gaia photometry for white dwarfs. *A&A*, v. 565, p. A11, maio 2014. Citado na página 28.

Cummings, J. D. et al. The White Dwarf Initial-Final Mass Relation for Progenitor Stars from 0.85 to 7.5 $M_{\odot}$. *ApJ*, v. 866, p. 21, out. 2018. Citado na página 31.

Dufour, P.; Bergeron, P.; Fontaine, G. Detailed Spectroscopic and Photometric Analysis of DQ White Dwarfs. In: Koester, D.; Moehler, S. (Ed.). *14th European Workshop on White Dwarfs*. [S.l.: s.n.], 2005. (Astronomical Society of the Pacific Conference Series, v. 334), p. 197. Citado na página 22.

Eisenstein, D. J. et al. A Catalog of Spectroscopically Confirmed White Dwarfs from the Sloan Digital Sky Survey Data Release 4. *ApJS*, v. 167, p. 40–58, nov. 2006. Citado 3 vezes nas páginas 22, 27, and 37.

Fontaine, G.; Brassard, P. The Pulsating White Dwarf Stars. *PASP*, v. 120, p. 1043, out. 2008. Citado na página 21.

Fontaine, G.; Wesemael, F. Recent advances in the theory of white dwarf spectral evolution. In: Philip, A. G. D.; Hayes, D. S.; Liebert, J. W. (Ed.). *IAU Colloq. 95: Second Conference on Faint Blue Stars*. [S.l.: s.n.], 1987. p. 319–326. Citado na página 25.

Fujimoto, M. Y. On the Origin of R-Type Carbon Stars: Possibility of Hydrogen Mixing during Helium Flicker. *PASJ*, v. 29, p. 331–350, 1977. Citado na página 23.

Garcia-Berro, E. et al. Properties of high-density binary mixtures and the age of the universe from white dwarf stars. *Nature*, v. 333, p. 642–644, jun. 1988. Citado na página 21.

Garcia-Berro, E. et al. Theoretical white-dwarf luminosity functions for two phase diagrams of the carbon-oxygen dense plasma. *A&A*, v. 193, p. 141–147, mar. 1988. Citado na página 21.

Green, R. F. The luminosity function of hot white dwarfs. *ApJ*, v. 238, p. 685–698, jun. 1980. Citado na página 34.

Hansen, B. M. S. et al. The White Dwarf Cooling Sequence of NGC 6397. *ApJ*, v. 671, p. 380–401, dez. 2007. Citado na página 21.

Hansen, B. M. S. et al. The White Dwarf Cooling Sequence of the Globular Cluster Messier 4. *ApJ*, v. 574, p. L155–L158, ago. 2002. Citado na página 21.

Iben JR., I. Stellar Evolution. I. The Approach to the Main Sequence. *ApJ*, v. 141, p. 993, abr. 1965. Citado na página 19.

Iben JR., I. On the frequency of planetary nebula nuclei powered by helium burning and on the frequency of white dwarfs with hydrogen-deficient atmospheres. *ApJ*, v. 277, p. 333–354, fev. 1984. Citado na página 23.

Iben JR., I.; MacDonald, J. The Born Again AGB Phenomenon. In: Koester, D.; Werner, K. (Ed.). *White Dwarfs*. [S.l.: s.n.], 1995. (Lecture Notes in Physics, Berlin Springer Verlag, v. 443), p. 48. Citado na página 23.

Kalirai, J. S. et al. Ultra-Deep Hubble Space Telescope Imaging of the Small Magellanic Cloud: The Initial Mass Function of Stars with M $<\tilde{}$ 1 M $_{???}$. *ApJ*, v. 763, p. 110, fev. 2013. Citado na página 21.

Kalirai, J. S. et al. The CFHT Open Star Cluster Survey. III. The White Dwarf Cooling Age of the Rich Open Star Cluster NGC 2099 (M37). *AJ*, v. 122, p. 3239–3257, dez. 2001. Citado na página 21.

Kepler, S. O. et al. White dwarf mass distribution in the SDSS. *MNRAS*, v. 375, p. 1315–1324, mar. 2007. Citado na página 34.

Kepler, S. O.; Koester, D.; Ourique, G. A white dwarf with an oxygen atmosphere. *Science*, v. 352, p. 67–69, abr. 2016. Citado na página 23.

Kepler, S. O. et al. New white dwarf stars in the Sloan Digital Sky Survey Data Release 10. *MNRAS*, v. 446, p. 4078–4087, fev. 2015. Citado 3 vezes nas páginas 22, 27, and 37.

Kepler, S. O. et al. New white dwarf and subdwarf stars in the Sloan Digital Sky Survey Data Release 12. *MNRAS*, v. 455, p. 3413–3423, fev. 2016. Citado 3 vezes nas páginas 22, 27, and 37.

Kilic, M. et al. The age of the Galactic stellar halo from Gaia white dwarfs. *MNRAS*, v. 482, p. 965–979, jan. 2019. Citado na página 21.

Kleinman, S. J. et al. A Catalog of Spectroscopically Identified White Dwarf Stars in the First Data Release of the Sloan Digital Sky Survey. *ApJ*, v. 607, p. 426–444, maio 2004. Citado 3 vezes nas páginas 22, 27, and 37.

Koester, D. White dwarf spectra and atmosphere models . *Mem. Soc. Astron. Italiana*, v. 81, p. 921–931, 2010. Citado na página 28.

Koester, D.; Kepler, S. O. DB white dwarfs in the Sloan Digital Sky Survey data release 10 and 12. *A&A*, v. 583, p. A86, nov. 2015. Citado na página 28.

Koester, D.; Weidemann, V.; Zeidler, E.-M. Atmospheric parameters and carbon abundance of white dwarfs of spectral types C2 and DC. *A&A*, v. 116, p. 147–157, dez. 1982. Citado na página 22.

Lauffer, G. R. *Evolutionary sequences for H and He atmosphere massive white dwarf stars*. Dissertação (Mestrado) — Universidade Federal do Rio Grande do Sul, 2018. Citado 2 vezes nas páginas 11 and 20.

Lauffer, G. R.; Romero, A. D.; Kepler, S. O. New full evolutionary sequences of H- and He-atmosphere massive white dwarf stars using MESA. *MNRAS*, v. 480, p. 1547–1562, out. 2018. Citado na página 19.

Legendre, A.; Gauss, C. F.; Laplace, P. *Least Square Method*. 1806,1809,1810. Citado na página 27.

Liebert, J.; Bergeron, P.; Holberg, J. B. The True Incidence of Magnetism Among Field White Dwarfs. *AJ*, v. 125, p. 348–353, jan. 2003. Citado na página 34.

Liebert, J.; Bergeron, P.; Holberg, J. B. The Formation Rate and Mass and Luminosity Functions of DA White Dwarfs from the Palomar Green Survey. *ApJS*, v. 156, p. 47–68, jan. 2005. Citado na página 31.

Limoges, M.-M.; Bergeron, P. A Spectroscopic Analysis of White Dwarfs in the Kiso Survey. *ApJ*, v. 714, p. 1037–1051, maio 2010. Citado na página 34.

MacDonald, J.; Hernanz, M.; Jose, J. Evolutionary calculations of carbon dredge-up in helium envelope white dwarfs. *MNRAS*, v. 296, p. 523–530, maio 1998. Citado na página 22.

Mestel, L. On the theory of white dwarf stars. I. The energy sources of white dwarfs. *MNRAS*, v. 112, p. 583, 1952. Citado na página 23.

Munn, J. A. et al. A Deep Proper Motion Catalog Within the Sloan Digital Sky Survey Footprint. *AJ*, v. 148, p. 132, dez. 2014. Citado na página 27.

Munn, J. A. et al. A Deep Proper Motion Catalog Within the Sloan Digital Sky Survey Footprint. II. The White Dwarf Luminosity Function. *AJ*, v. 153, p. 10, jan. 2017. Citado na página 27.

Pelletier, C. et al. Carbon pollution in helium-rich white dwarf atmospheres Time-dependent calculations of the dredge-up process. *ApJ*, v. 307, p. 242–252, ago. 1986. Citado na página 22.

Rebassa-Mansergas, A. et al. Post-common envelope binaries from SDSS-X: the origin of low-mass white dwarfs. *MNRAS*, v. 413, p. 1121–1131, maio 2011. Citado na página 31.

Rebassa-Mansergas, A. et al. The mass function of hydrogen-rich white dwarfs: robust observational evidence for a distinctive high-mass excess near 1 M???. *MNRAS*, v. 452, p. 1637–1642, set. 2015. Citado na página 34.

Rolland, B.; Bergeron, P.; Fontaine, G. On the Spectral Evolution of Helium-atmosphere White Dwarfs Showing Traces of Hydrogen. *ApJ*, v. 857, p. 56, abr. 2018. Citado 2 vezes nas páginas 25 and 37.

Romero, A. D.; Campos, F.; Kepler, S. O. The age-metallicity dependence for white dwarf stars. *MNRAS*, v. 450, p. 3708–3723, jul. 2015. Citado 3 vezes nas páginas 19, 31, and 41.

Romero, A. D. et al. Toward ensemble asteroseismology of ZZ Ceti stars with fully evolutionary models. *MNRAS*, v. 420, p. 1462–1480, fev. 2012. Citado 3 vezes nas páginas 11, 21, and 41.

Schlegel, D. J.; Finkbeiner, D. P.; Davis, M. Maps of Dust Infrared Emission for Use in Estimation of Reddening and Cosmic Microwave Background Radiation Foregrounds. *ApJ*, v. 500, p. 525–553, jun. 1998. Citado na página 27.

Schmidt, M. Space Distribution and Luminosity Functions of Quasi-Stellar Radio Sources. *ApJ*, v. 151, p. 393, fev. 1968. Citado na página 34.

Schmidt, M. The mass of the galactic halo derived from the luminosity function of high-velocity stars. *ApJ*, v. 202, p. 22–29, nov. 1975. Citado na página 34.

Schneider, A. S. et al. Phase diagram of carbon-oxygen plasma mixtures in white dwarf stars. In: *Journal of Physics Conference Series*. [S.l.: s.n.], 2012. (Journal of Physics Conference Series, v. 402), p. 012026. Citado na página 21.

Schoenberner, D. Asymptotic giant branch evolution with steady mass loss. *A&A*, v. 79, p. 108–114, out. 1979. Citado na página 23.

Shipman, H. L. Properties and evolution of white dwarf stars. In: Torres-Peimbert, S. (Ed.). *Planetary Nebulae*. [S.l.: s.n.], 1989. (IAU Symposium, v. 131), p. 555–566. Citado na página 25.

Smartt, S. J. Progenitors of Core-Collapse Supernovae. *ARA&A*, v. 47, p. 63–106, set. 2009. Citado na página 19.

Stobie, R. S.; Ishida, K.; Peacock, J. A. Distance errors and the stellar luminosity function. *MNRAS*, v. 238, p. 709–727, maio 1989. Citado na página 34.

Torres, S. et al. High-proper-motion white dwarfs and halo dark matter. *MNRAS*, v. 336, p. 971–978, nov. 2002. Citado na página 21.

Tremblay, P.-E.; Bergeron, P. The Ratio of Helium- to Hydrogen-Atmosphere White Dwarfs: Direct Evidence for Convective Mixing. *ApJ*, v. 672, p. 1144–1152, jan. 2008. Citado 5 vezes nas páginas 13, 36, 37, 40, and 41.

Tremblay, P.-E.; Bergeron, P.; Gianninas, A. An Improved Spectroscopic Analysis of DA White Dwarfs from the Sloan Digital Sky Survey Data Release 4. *ApJ*, v. 730, p. 128, abr. 2011. Citado na página 41.

van Horn, H. M. Evolutionary Implications of the Crystallization of White Dwarfs. *AJ*, v. 72, p. 834, out. 1967. Citado na página 23.

Winget, D. E. et al. An independent method for determining the age of the universe. *ApJ*, v. 315, p. L77–L81, abr. 1987. Citado na página 21.

Winget, D. E.; Kepler, S. O. Pulsating White Dwarf Stars and Precision Asteroseismology. *ARA&A*, v. 46, p. 157–199, set. 2008. Citado na página 21.

Winget, D. E. et al. The Physics of Crystallization From Globular Cluster White Dwarf Stars in NGC 6397. *ApJ*, v. 693, p. L6–L10, mar. 2009. Citado na página 21.

Woosley, S. E.; Heger, A. The Remarkable Deaths of 9-11 Solar Mass Stars. *ApJ*, v. 810, p. 34, set. 2015. Citado na página 19.

Yuan, H. B.; Liu, X. W.; Xiang, M. S. Empirical extinction coefficients for the GALEX, SDSS, 2MASS and WISE passbands. *MNRAS*, v. 430, p. 2188–2199, abr. 2013. Citado na página 27.

APPENDIX A – Published Paper

MNRAS **000**, 1–9 (2018) Preprint 10 October 2018 Compiled using MNRAS LATEX style file v3.0

A Study of Cool White Dwarfs in the Sloan Digital Sky Survey Data Release 12

G. Ourique,[1] A. D. Romero,[1] S. O. Kepler,[1] D. Koester,[2] L. A. Amaral[1]
[1] *Instituto de Física, Universidade Federal do Rio Grande do Sul, 91501-900 Porto-Alegre, RS, Brazil*
[2] *Institut für Theoretische Physik und Astrophysik, Universität Kiel, 24098 Kiel, Germany*

Accepted XXX. Received YYY; in original form ZZZ

ABSTRACT

In this work we study white dwarfs where 30 000 K>$T_{\rm eff}$>5 000 K to compare the differences in the cooling of DAs and non-DAs and their formation channels. Our final sample is composed by nearly 13 000 DAs and more than 3 000 non-DAs that are simultaneously in the SDSS DR12 spectroscopic database and in the *Gaia* survey DR2. We present the mass distribution for DAs, DBs and DCs, where it is found that the DCs are ∼0.15 $M_\odot$ more massive than DAs and DBs on average. Also we present the photometric effective temperature distribution for each spectral type and the distance distribution for DAs and non-DAs. In addition, we study the ratio of non-DAs to DAs as a function of effective temperature. We find that this ratio is around ∼0.075 for effective temperature above ∼22 000 K and increases by a factor of five for effective temperature cooler than 15 000 K. If we assume that the increase of non-DA stars between ∼22 000 K to ∼15 000 K is due to convective dilution, 14±3 per cent of the DAs should turn into non-DAs to explain the observed ratio. Our determination of the mass distribution of DCs also agrees with the theory that convective dilution and mixing are more likely to occur in massive white dwarfs, which supports evolutionary models and observations suggesting that higher mass white dwarfs have thinner hydrogen layers.

Key words: white dwarfs – catalogues – proper motions

1 INTRODUCTION

White dwarf stars (WDs) are the result of the stellar evolution for stars with initial masses below $7-10.6\,M_\odot$, depending on the initial metalicity (Ibeling & Heger 2013; Doherty et al. 2015; Woosley & Heger 2015). This correspond to 97 per cent of the stars in the Milky Way (Winget & Kepler 2008; Fontaine & Brassard 2008; Althaus et al. 2010). WDs are abundant and long-lived objects so they convey information about all galactic populations (Isern et al. 2001; Liebert et al. 2005; Bono et al. 2013). A particular feature of WDs is that their evolution is predominantly a simple cooling, so they can be considered reliable cosmic clocks to infer the age of a wide variety of stellar populations, such as the Galactic discs and halo (Winget et al. 1987; Garcia-Berro et al. 1988a,b; Torres et al. 2002), and globular and open clusters (Kalirai et al. 2001; Hansen et al. 2002, 2007; Kalirai et al. 2013; Campos et al. 2016).

WDs having atmospheres dominated by hydrogen, with optical spectra dominated by strong Balmer lines, are known as DAs and correspond to ≈83 per cent of the known sample of spectroscopically confirmed WDs (Kleinman et al. 2004; Eisenstein et al. 2006; Kepler et al. 2015, 2016b). WDs with spectra not dominated by hydrogen lines are known as non-DAs and can be divided into distinct sub-classes depending on the objects effective temperature and the observed spectral lines (Sion et al. 1983). Around 7 per cent of the known spectroscopic WDs have their spectra dominated by helium lines, known as DOs if they are hot enough to show He II lines and DBs if they only show He I lines (e.g. Koester & Kepler 2015). Around 5 per cent of known spectroscopic WDs are too cool to show absorption lines in their optical spectra. These objects are known as DCs, and usually assumed to have atmospheres dominated by helium if the effective temperature is above 5 000 K, inferred from the fact that hydrogen lines should be seen at those temperatures, if hydrogen is present in the atmosphere (Bergeron et al. 1997, 2001). Around 1 per cent of the known WD stars present carbon lines or bands, depending on the effective temperature. WDs with atmospheres polluted or dominated by oxygen (DS) are know, but they are not statistically significant (Gänsicke et al. 2010; Kepler et al. 2016a). The class of WDs showing metal lines other than carbon or oxygen in their spectra are known as DZs. These metal polluted WDs correspond to 4 per cent of the known WDs. The spectra of DZs usually show hydrogen or helium lines if these elements

are present in the atmosphere and the effective temperature is above 5 000 K or 12 000 K, respectively. The metal content in the atmosphere of DZs is understood to come from ongoing accretion, since any metal from the progenitor composition will sink towards the centre of the star due to gravitational settling on time scales shorter than the WD evolutionary time scales (e.g. Koester et al. 2011). In addition, the accretion of hydrogen (or water) through the accretion of planetesimals can also influence the spectral class of WDs (Gentile Fusillo et al. 2017).

Tremblay & Bergeron (2008) estimated the helium to hydrogen atmosphere WD number ratio as a function of effective temperature from a model atmosphere analysis of the infrared photometric data from the 2MASS survey. Their sample comprised 340 hydrogen-rich atmosphere WDs and 107 helium-rich atmosphere WDs with spectroscopic effective temperatures in the range 15 000 K>$T_{\rm eff}$>5 000 K. Their focus was to study the impact of hydrogen convective mixing. They proposed that about 15 per cent of the DAs are transformed into non-DAs at lower temperatures due to convective mixing in thin hydrogen envelope stars, where thin envelope is defined as hydrogen layer masses below $\approx 10^{-8} M_*$, with M_* being the stellar mass. With a total sample of 447 WDs in their effective temperature range, they estimated that the helium to hydrogen atmosphere WD number ratio increases from 0.25 at 15 000 K to 0.45 at 6 000 K.

From single stellar evolution, the hydrogen layer mass not burnt in a WD should be around $\approx 10^{-4} M_*$ for canonical stellar masses of $\approx 0.6\,M_\odot$, being thinner for higher masses (see Paczyński 1971; Renedo et al. 2010; Romero et al. 2012). Values below $\approx 10^{-8} M_*$ require an additional hydrogen-depleting mechanism acting on the external layers of the stars. Strong evidence for the existence of a hydrogen layer mass range in WDs comes from asteroseismology. For instance, Castanheira & Kepler (2009), studying a sample of 83 ZZ Ceti stars, found the surface hydrogen layer to range from $10^{-10} < M_H/M_* < 10^{-4}$, with an average value of 2.71×10^{-5}. Romero et al. (2012), using asteroseismology based on full evolutionary models, analysed a sample of 44 ZZ Ceti stars with stellar masses from $\sim 0.5\,M_\odot$ to $\sim 0.8\,M_\odot$ and also found a broad range of hydrogen-layer thickness, with a similar average for the hydrogen mass. From their sample, 20 per cent of the stars showed a hydrogen layer thinner than predicted by single stellar evolution, and 13 per cent showed hydrogen layers below $M_H/M_* = 10^{-8}$. Thus, there are several pieces of evidences for mixing and spectral evolution in WDs, imprinted in the DA and non-DA samples, that could be studied in detail if a statistically significant sample of WDs is available.

In recent years, the number of spectroscopically confirmed WD stars has dramatically increased, in particular due to the Sloan Digital Sky Survey (SDSS) project. SDSS is one of the largest photometric and spectroscopic surveys, having more than 1.0 billion objects with observed photometry and more than 4.8 million with spectra obtained in Data Release 14 (Abolfathi et al. 2017). More than 30 000 spectroscopically confirmed new WD stars have been found within the SDSS until Data Release 12 (Kleinman et al. 2004; Eisenstein et al. 2006; Kleinman et al. 2013; Kepler et al. 2015, 2016b).

With the *Gaia* Data Release 2 (Luri et al. 2018), the parallaxes of most of the known spectroscopically identified WDs have been determined, providing a direct distance determination for all objects in our sample, and allowing a better estimate of effective temperature and gravity for cool WDs that do not show significant spectral lines.

In this work, we take advantage of the large sample of spectroscopically confirmed WDs with measured distances to study the spectral evolution in WDs and its possible origin. We compute the distances for an initial sample of 19 023 WDs cooler than 30 000, K from SDSS DR12 using *Gaia* parallaxes, and from their colours we estimate their photometric effective temperature. Because the synthetic colour grid used for parameter determination in this work assumes $\log g = 8.0$ dex for DZs and DQs (Koester 2010; Koester & Kepler 2015) we only estimate the stellar mass for the DAs, DBs and DCs. Furthermore, we only consider DAs, DBs and DCs with estimated mass above $0.45\,M_\odot$ to avoid objects that originate from interacting binaries.

Our final sample has 17 215 objects, with 13 678 DAs, 1 528 DBs, 1 173 DCs, 557 DZs and 279 DQs. With this sample we compute the helium to hydrogen atmosphere WD number and density ratio for WDs in the range of effective temperatures 30 000 K>$T_{\rm eff}$>5 000 K.

This paper is organised as follows: In Section 2 we present our data sample and classification. Section 3 is devoted to mass and photometric effective temperature determination. In Section 4 we discuss the spatial distribution and completeness while in Section 5 we present our calculation of the helium to hydrogen atmosphere WD ratio. Discussion and conclusions are presented in Section 6.

2 DATA SAMPLE

Our analysed objects are taken from the WD catalogues based on SDSS data of Kleinman et al. (2004); Eisenstein et al. (2006); Kepler et al. (2015, 2016b). We select all objects classified as single WDs with DA, DB, DC, DZ and DQ spectral type with determined effective temperature in the range 30 000 K>$T_{\rm eff}$>5 000 K.

To extend our spectroscopic sample to lower effective temperatures we include the WDs in the Munn et al. (2014) deep proper motion catalogue. Munn et al. (2017) classified a sample of 8 472 objects in the deep proper motion catalogue as possible WDs using SDSS colours. Note that, since the cool WDs are intrinsically faint, they must be nearby and thus should have high proper motion. Of their 8 472 objects, 2 144 have spectroscopic observations from SDSS and 1 668 were also found in the catalogue presented in Kepler et al. (2016b, 2015); Eisenstein et al. (2006); Kleinman et al. (2004). Using the spectra from SDSS, we determine the spectral class of the 476 objects from Munn et al. (2017) that were not included in the SDSS WD catalogues and found that 395 of these objects are WDs in the effective temperature range considered in this work.

As a result, our initial sample is composed of 17 492 DAs, 1 766 DBs, 1 290 DCs, 557 DZs and 279 DQs, totaling 21 384 WDs.

3 PARAMETER DETERMINATION

To determine the parameters characterising each object, we consider magnitudes from filters u, g, r, i and z of the SDSS photometric catalogue (Gunn et al. 1998; Doi et al. 2010) de-rredened with Schlegel et al. (1998) reddening maps and using Yuan et al. (2013) extinction coefficients in addition to *Gaia* parallaxes (Luri et al. 2018). To take into account the asymmetric uncertainties for each parameter, the parallaxes are randomly sampled assuming that the measured values are the mean values and their uncertainties are the standard deviation of a normal distribution. The sampling is repeated 1 000 times for each object and then the distance is calculated from each sampled parallax. This procedure generates a Monte Carlo probability density for distances. For each star we use the median of the probability distribution as the distance and the difference of 16% and 84% with the median as the lower and upper uncertainty, respectively.

The same Monte Carlo procedure is used to sample over the magnitudes and their respective uncertainties to compute colours, which are fitted to a synthetic colour grid from Koester (2010); Koester & Kepler (2015) using a least squares method. We determine the absolute magnitude of synthetic colour models using the luminosity provided by Carrasco et al. (2014) models. The least squares fitting is limited to models where the photometric distances for all filters agree with the parallax distance within one sigma. This procedure generates a Monte Carlo probability density for each parameter, i.e. effective temperature and absolute magnitudes. For DAs we used synthetic colours for hydrogen-rich, while for DBs and DCs we used helium-rich atmosphere WD models. For DQs and DZs we used synthetic colours for carbon-rich and metal-rich atmosphere WD models that assumes $\log g$=8.0 and have abundances within 4<[C/He]<10 and 7<[Z/He]<10.5, respectively. For DQs and DZs models, the SDSS u, g, r, i and z do not depend on metallicity for $T_{\rm eff}$>10 000 K, but there is a dependence at lower temperatures, reaching one magnitude for u and 0.5 magnitude for z at 5 000 K. Due to the fixed $\log g$ of our atmosphere models, we could not estimate the mass of DQs and DZs.

For DAs, DBs and DCs the stellar masses are estimated from the distance and effective temperature of each object, which determines their luminosity and radii, through the mass-radius relation provided by Carrasco et al. (2014) synthetic colour model grid that assumes hydrogen layer mass $M_H/M_*= -4$ and helium layer mass $M_H/M_*= -2$ (e.g. Hamada & Salpeter 1961; Koester 1978; Provencal et al. 1998; Tremblay et al. 2017).

An example of the Monte Carlo probability density for the determination of the photometric effective temperature can be seen in Figure 1 for *SDSS J234212.45+044531.7*. We include in the figure, with a vertical blue line, the spectroscopic determination. The determined uncertainties are internal to our method and the photometric data, not including the uncertainties related to the synthetic colour models.

3.1 Masses

We computed the stellar mass for all objects in our sample classified as DAs, DBs or DCs. Then we calculated the mass distribution for each spectroscopic class, shown in Figure 2. Since we have asymmetric uncertainties that reach up to

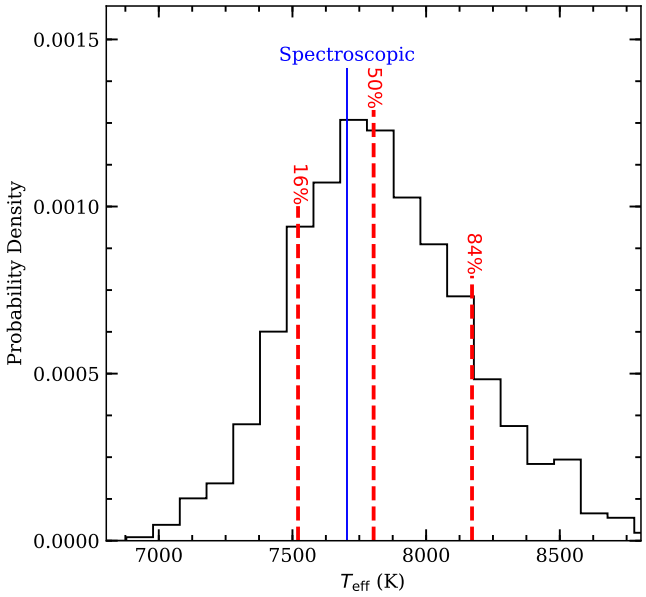

Figure 1. Distribution of photometric effective temperature determined with our Monte Carlo method and its uncertainty for the DAs *SDSS J234212.45+044531.7*. The red dashed lines represent 16, 50 and 84 percentiles while the blue solid line is the spectroscopically determined effective temperature from Kleinman et al. (2013). Our determination is 7804^{+368}_{-283} K, agreeing within uncertainties with the spectroscopic determination, 7704 ± 56 K. The SDSS magnitude in filter g for this object is 19.460 ± 0.019 and the signal to noise ratio for the spectrum is 16 in filter g.

25 per cent of the estimated value for several objects, we used Monte Carlo methods to include this information in our distributions. Due to the large uncertainties, the study of individual objects is not reliable in this work. However, our sample is large enough for a statistically significant study. The width of our distributions come mostly from the high uncertainties on mass determinations.

From Figure 2 we can see that the distribution in mass for DAs and DBs are very similar. The main difference between the DA and DB distributions is the higher number of counts for lower and higher masses present in the DAs mass distribution. On the other hand, the mass distribution for DCs is more concentrated towards higher masses, having a peak around ∼0.7 $M_\odot$, instead of ∼0.55 $M_\odot$ like DAs and DBs.

Our DA sample is much larger than our DB sample and the uncertainty in mass for each object is nearly the same for both samples. We conclude that the higher counts in the wings in the DAs mass distribution are not due to uncertainties, but come from a real excess in the number of DAs at higher and lower stellar masses. Our most acceptable explanation for these objects is that they come from interacting binaries where the increase or decrease of the total mass depends on its evolution (e.g. Kepler et al. 2007). This binary population is not expected in the DBs sample because binary evolution of a system containing a DB WD usually turn the helium–atmosphere component into a DA WD due to hydrogen accretion. Also a pure helium companion, or DB-DB system, is not common enough to produce a significant number of objects (see Yungelson 2008).

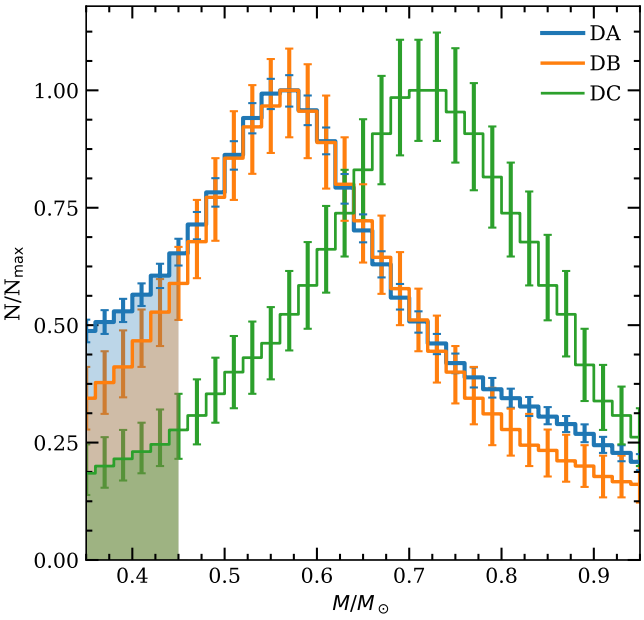

Figure 2. Mass distribution for DAs (blue), DBs (orange) and DCs (green). The DA and DB distributions have a peak around$\sim$0.55 $M_\odot$, but the DA distribution shows higher counts in the wings of the distribution. The DCs are essentially more massive than DAs and DBs, having a peak around $\sim$0.7 $M_\odot$. The shaded regions indicate objects that originated from interacting binaries, since any object with mass below 0.45 $M_\odot$ would not have time to turn into a WD by single star evolution given the age of the Universe.

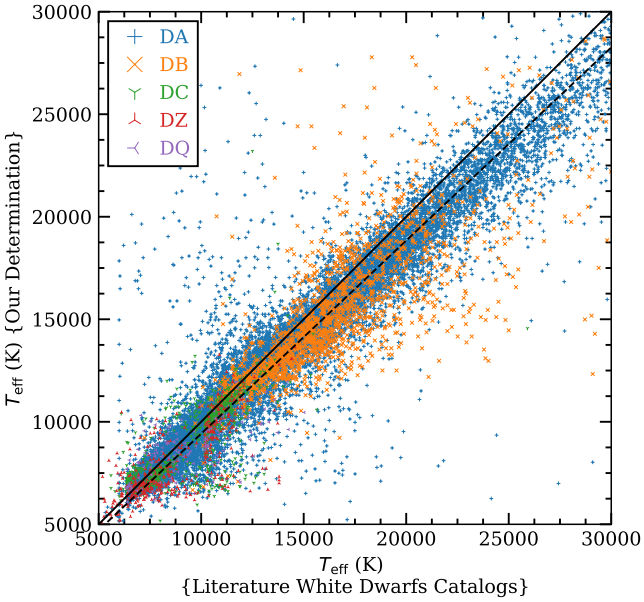

Figure 3. Comparison of the effective temperature determined in this work with the spectroscopic determination from Kleinman et al. (2004); Eisenstein et al. (2006); Kleinman et al. (2013); Kepler et al. (2015, 2016b). The solid black line is the identity line, while the dashed black line is the linear fit result. In colours blue, orange, green, red and purple we have the comparison for respective spectral classes: DA, DB, DC, DZ and DQ. The linear fit result indicates that our determinations are on average $\sim$6, $\sim$8, $\sim$6, $\sim$10 and $\sim$10 per cent cooler than the spectroscopic ones for DAs, DBs, DCs, DZs and DQs, respectively. Objects with spectroscopic determinations near to their spectroscopic model grid limit are not included.

Since any WD that has a stellar mass below $\sim$0.45 $M_\odot$ would take more than the age of the Universe to form through normal single star evolution (Liebert et al. 2005; Rebassa-Mansergas et al. 2011), we do not included objects of our sample with determined mass below 0.45 $M_\odot$ to avoid binary contaminants, reducing our final sample of DAs, DBs and DCs to, 13 678, 1 428 and 1 173 objects, respectively.

3.2 Photometric Effective Temperature

In this work we determine the photometric effective temperature for our entire sample. In this way we eliminate possible effects produced by the different effective temperature determination methods or model grids used in distinct catalogues.

We compare our determinations of the effective temperature with the spectroscopic values from Kleinman et al. (2004); Eisenstein et al. (2006); Kleinman et al. (2013); Kepler et al. (2015, 2016b) and with the photometric determination of Munn et al. (2017). The results are shown in Figure 3. Objects with spectroscopic effective temperature in the border of their spectroscopic models grid are not included in this figure. In the Figure 3 is also plotted the identity (solid black line) and the linear fit result (dashed black line), indicating that our determinations are on average $\approx$6 per cent cooler than the determinations from spectroscopy. The large difference in the determination of effective temperature for bright WDs is expected due the lack of spectral energy distribution information for shorter wavelengths when we use only SDSS photometric filters. These differences are not relevant for our DA to non-DA ratio determination, since they effect both samples similarly.

The distribution in photometric effective temperature for DAs, DBs, DCs, DZs and DQs normalised by the number of objects in each class can be seen in Figure 4. Note that for DCs, DZs and DQs most objects are found at effective temperatures below 11 000 K, while DBs are found above this effective temperature. On the other hand, the DAs are found in the entire effective temperature range.

The increase in the number of WDs at lower temperatures is expected because the cooling rate decreases as they cool. The times spent at low temperatures is therefore comparatively long. Due to their lower luminosities, a lower completeness in the number of WDs is expected at lower effective temperatures. For DBs, the peak occurs at higher effective temperatures because DBs turn into DCs at effective temperatures lower than 12 000 K as the He lines become undetectable at signal to noise ratio $\sim$10.

In this work, we consider as helium-rich atmosphere WDs all stars classified as DB, DC and DZ with effective temperatures in the range 30 000 K>T_{eff}>5 000 K, since objects with hydrogen in their atmospheres should present hydrogen lines within this temperature range (e.g. Koester et al. 2011). DQs are also considered as helium-rich atmosphere WDs because they do not present hydrogen lines and the carbon content is probably due to dredge-up processes (Koester et al. 1982; Pelletier et al. 1986; MacDonald

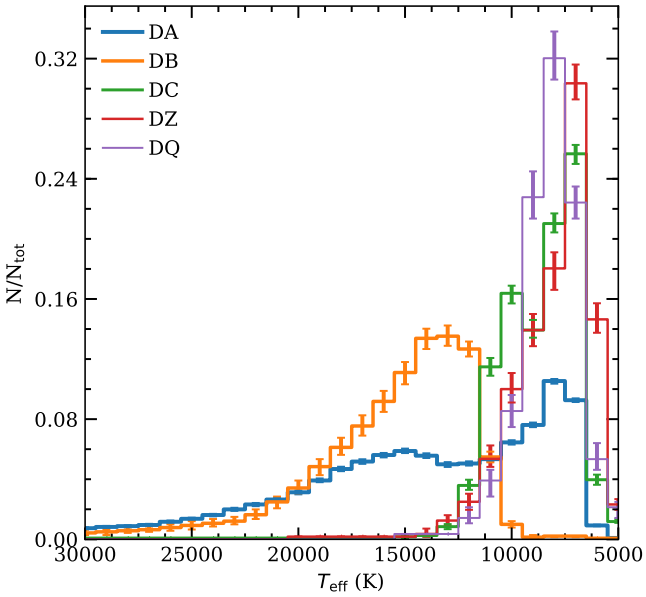

Figure 4. Our distribution of photometric effective temperature for DAs (blue), DBs (orange), DCs (green), DZs (red) and DQs (purple) in our sample. The bin width of all our distributions is 1 000 K and the effective temperature on the figure increase from right to left.

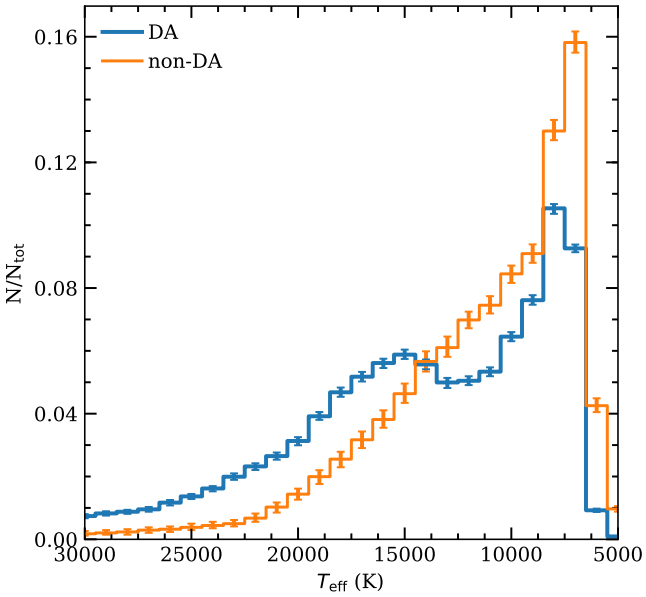

Figure 5. Photometric effective temperature distribution for DAs (blue) and non-DAs (orange). A change in the slope of the non-DA distribution can be seen around 21 000 K, with the number of stars increasing faster for lower temperatures. The DA distribution presents a lack of stars between 14 000 K and 12 000 K. The decrease in the number of counts for both distributions near to 5 000 K are due the incompleteness of the sample and the age of the disk. Both distributions are normalised by the total number of counts.

et al. 1998; Brassard et al. 2007; Dufour et al. 2005). Therefore we define as helium-rich atmosphere WDs all non-DAs from our sample. With these considerations, we study a final sample with 12 811 DAs and 3 374 non-DAs.

The photometric effective temperature distributions for DAs and non-DAs are depicted in Figure 5, normalised by the highest number of counts. From this figure we note that the non-DA distribution shows a change in the slope around 21 000 K, making the number of counts increase faster until ∼7 000 K, where there is a peak in the distribution. On the other hand, the DA distribution show a decrease in the slope around 15 000 K followed by a sudden decrease between 14 000 K and 12 000 K, and then increasing until ∼7 000 K. Both distributions show a decrease around 5 000 K due to the incompleteness of the sample and the age of the disk. Our uncertainties on the distributions are calculated using Monte Carlo methods.

4 DISTANCE DISTRIBUTION AND COMPLETENESS

We compute the distance distribution of DAs and non-DAs using the distances determined from *Gaia* parallaxes. As can be seen in Figure 6, the non-DA distribution is narrower than the DA distribution. The DA distribution has an extended tail to higher distances. As we are working with cool WDs that have spectroscopy in SDSS DR12, we expect a lower completeness for objects at higher distances or lower luminosities plus the saturation limit at magnitudes ∼14.5 on the g filter.

The scale-height of the galactic disk is around 300 pc (Kepler et al. 2017) and the peaks of both of our distance distributions are around 200 pc. Thus we notice that

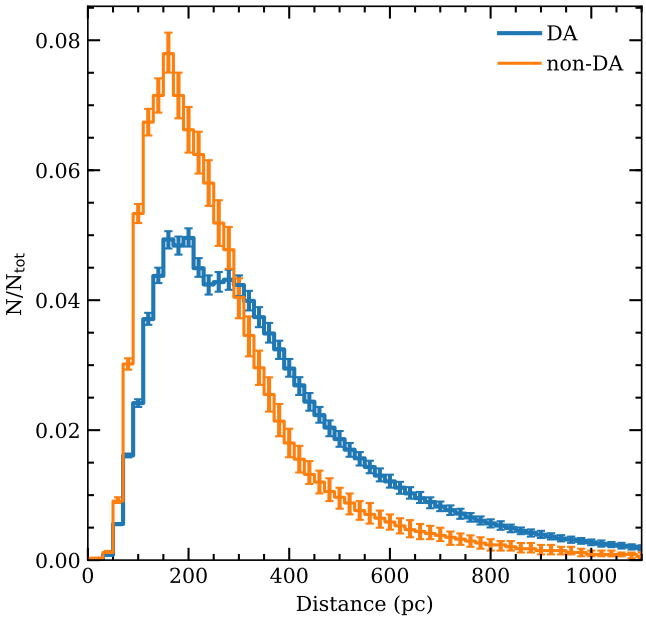

Figure 6. Distance distribution for DAs (blue) and non-DAs (orange). The non-DA distribution shows significantly more stars concentrated around 200 pc than the DAs distribution, which shows an extended tail to higher distances.

our analysis could be influenced by the incompleteness of our sample. The cumulative distance distribution for our DA and non-DA samples follow a cubic rule up to 110 pc, indicating that our sample should be near complete up to this distance in the SDSS spectroscopic cone (Oswalt et al. 2016; Holberg et al. 2016). To ensure the reliability of our results we present our determinations for a close to complete sample corrected by the observed volume, following Schmidt (1968, 1975); Green (1980); Stobie et al. (1989); Liebert et al. (2003); Kepler et al. (2007); Limoges & Bergeron (2010); Rebassa-Mansergas et al. (2015), limiting the magnitude on SDSS filter g, $14.5 < m_g < 19.0$, and assuming a galactic disk scale height of 300 pc. The resulting sample after applying the magnitude limits for the correction is composed of 5 336 DAs and 1 315 non-DAs.

4.1 Volume Corrected Distributions

Figure 7 shows the volume corrected mass distribution for DAs, DBs and DCs, as well as the sum of the three distributions. In this figure we see an overdensity of DAs for masses higher than $\sim$0.75 $M_\odot$. This overdensity could be explained if a burst of star formation occurred within the last 0.5 Gyr, considering single stellar evolution, since it shows a stellar mass distribution concentrated around $\sim$0.87 $M_\odot$. This scenario is not very probable, since the number of objects that should be formed in less than 0.5 Gyr is too high. A more likely scenario involves mergers, that result in high mass WDs. The low mass binary component, also shown in Figure 2, is not as prominent in Figure 7, since low mass WDs have higher radius and could be seen at much higher distances. Also we can see that DBs are not very significant for the total distribution, which is expected considering that they are intrinsically hot WDs. For DCs, we see an important contribution to the total number for lower effective temperatures, showing an increase in the number of objects for higher masses. Note that the number of DAs decreases in the same way as the number of DCs increases, indicating that some massive DAs could be turning into massive DCs.

Figure 8 shows the volume corrected effective temperature distributions for DA and non-DAs. From this figure we see that both distributions show a decrease in the density around 5 000 K, and present the same slope, indicating that the two samples have nearly the same age. Also we determine from the volume corrected effective temperature distribution that around 30±1 per cent of the total WDs are non-DAs.

In Figure 9 we show the volume corrected distance distribution for DAs and non-DAs after applying the volume correction, normalised by the sum of weights resulting from the correction. We can see that DAs and non-DAs follow nearly the same distance distribution.

For a uniform distribution along the galactic disk, we expect the mean of the volume calculated at each star distance over the maximum volume at which this star could be seen, i.e $V/V_{\rm max}$, to be around 0.5. For our DAs and non-DAs samples we found that $V/V_{\rm max}$ is, respectively, 0.51 and 0.50. This means that within these magnitude limits both distributions follow a nearly uniform distribution.

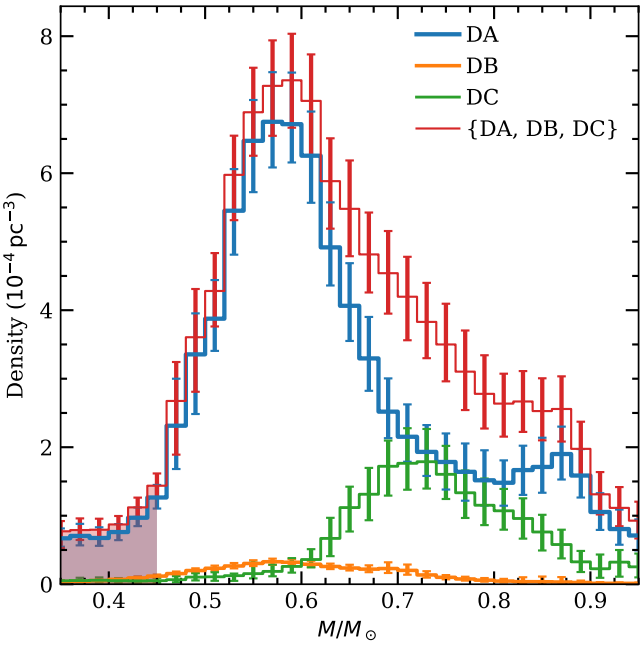

Figure 7. Mass distribution for DAs (blue), DBs (orange), DCs (green) and the sum of the three distributions (red). The peak at higher masses in the DA distribution indicates a population that could have come from mergers. Due their higher luminosities, DBs are not significant in volume corrected distribution. On the other hand, due the low radius and effective temperature of DCs, they correspond to 36 per cent of the density of WDs above $\sim$0.7 $M_\odot$, but only 12 per cent in number.

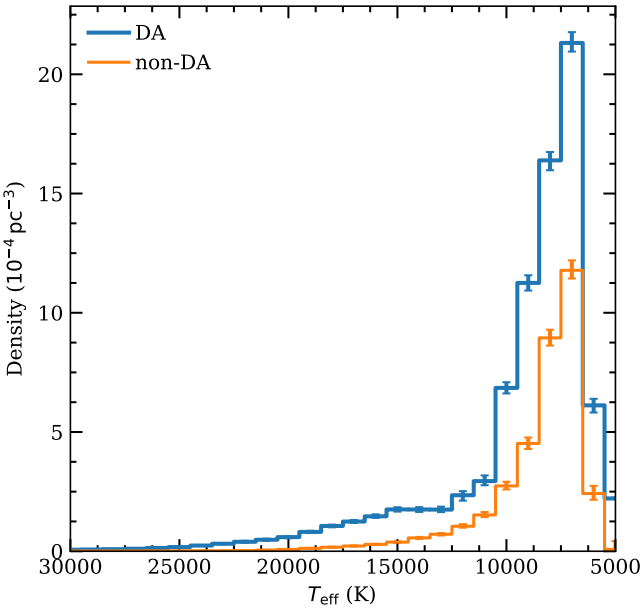

Figure 8. Photometric effective temperature distribution for DAs (blue) and non-DAs (orange). The decrease in the density of objects for both distributions around 5 000 K indicates that they have the same maximum age.

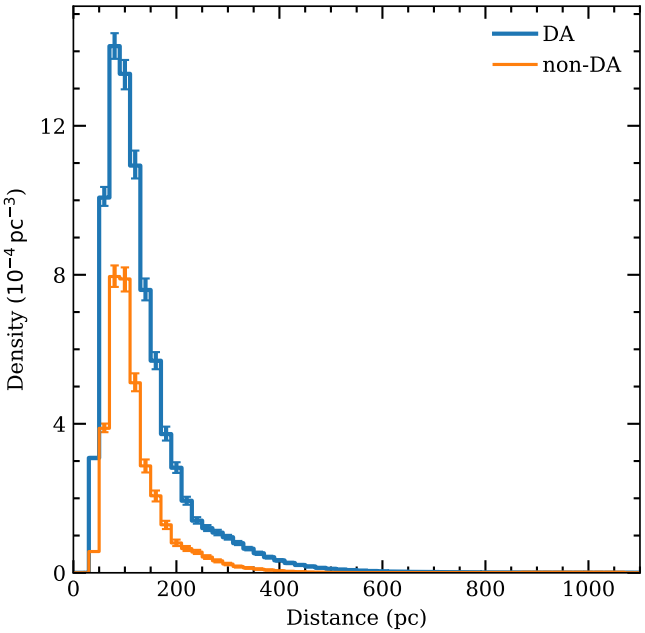

Figure 9. Distance distribution for DAs (blue) and non-DAs (orange) WDs after applying the volume correction. Our sample do not present any object closer than 30 pc due the SDSS saturation limits. Both distributions are normalised by the sum of weights resulting from the correction.

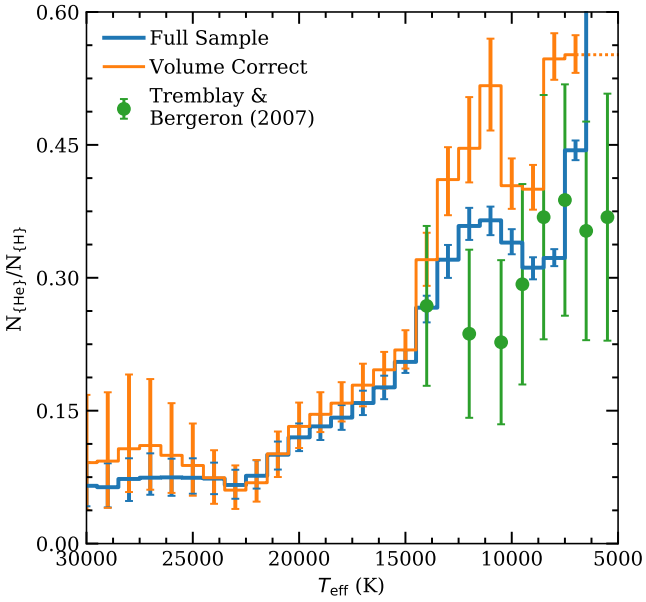

Figure 10. Helium to hydrogen atmosphere WD number ratio as a function of the effective temperature calculated with our final sample of 12 811 DAs and 3 374 non-DAs (blue), the density ratio calculated with our volume corrected sample of 4 775 DAs and 1308 non-DAs (orange) and the ratio calculated by Tremblay & Bergeron (2008) (green). The effective temperature increases from right to left. Our determinations are for effective temperatures in the range 30 000 K>T_{eff}>5 000 K, while the determination of Tremblay & Bergeron (2008) is in the range 15 000 K>T_{eff}>5 000 K. Our determinations show that the helium to hydrogen atmosphere WD number ratio shows an increase of more than 4 times the ratio for effective temperatures between 21 000 K and 12 500 K, followed by a decrease around ≈10 000 K and then a large increase around 5 000 K, where DAs and non-DAs become practically indistinguishable.

5 HELIUM TO HYDROGEN ATMOSPHERE WD NUMBER AND DENSITY RATIO

An efficient way to study the difference between the DAs and non-DAs is through the helium to hydrogen number ratio, defined as the ratio between the number or density of helium-rich to hydrogen-rich atmosphere WDs as a function of the effective temperature. This quantity will give information on the differences on the formation and evolutionary channels of these two populations of WDs (Tremblay & Bergeron 2008).

Figure 10 depicts the helium to hydrogen atmosphere WD number ratio calculated with our final sample of 13 687 DAs and 3 437 non-DAs (blue line) and the density ratio calculated with our volume corrected sample of 5 336 DAs and 1 315 non-DAs (orange line). Also shown in Figure 10 is the ratio calculated by Tremblay & Bergeron (2008) (green points). Note that, for both of our determinations, the helium to hydrogen atmosphere WD number ratio starts to increase significantly at effective temperatures around 22 000 K, where the convection in the helium layers becomes adiabatic (e.g. Althaus et al. 2010). Figure 10 also presents a second increase around ≈14 000 K, which coincides with the temperature when the hydrogen convective layer starts to develop according to theoretical models. This increase is followed by a decrease around ≈10 000 K and then a large increase around 5 000 K, where DAs and non-DAs become practically indistinguishable in optical spectra. Tremblay & Bergeron (2008) computed the helium to hydrogen atmosphere WD number ratio only in the effective temperature range 15 000 K>T_{eff}>5 000 K, using a sample of 340 DAs and 107 non-DAs (green dots in Figure 10), and found a factor of two increase in the helium to hydrogen atmosphere WD number ratio for effective temperatures around 10 000 K, which they explained by stating that 15 per cent of the DAs turn into non-DAs for effective temperatures between 15 000 K and 10 000 K. This result could be explained by the occurrence of convective mixing in the outer layers for WDs with hydrogen content, M_H/M_*, below 10^{-8}.

Our determination of the helium to hydrogen atmosphere WD number and density ratio in the same effective temperatures range studied by Tremblay & Bergeron (2008) does not lead to the same conclusion, since the increase in the ratio around 10 000 K that they found is not seen in our data. We believe this effect could be related to the small number of objects considered in their analysis or their choice of their upper effective temperature limit and not to a property of the helium to hydrogen atmosphere WD number ratio itself.

Rolland et al. (2018) propose that the convective dilution of a hydrogen layer with $\log M_H/M_\odot \sim -14$ will occur for effective temperatures near 20 000 K and no more than 32 000, K, turning DAs into non-DAs. In Figure 10 we can see an increase helium to hydrogen atmosphere WD number and density ratio at effective temperatures 22 000 K, which is possible evidence of convective dilution. Spectroscopic catalogues reported approximately 250 DABs around 24 000 K (Kepler et al. 2016b, 2015; Eisenstein et al. 2006;

Kleinman et al. 2004), very close to where we found an increase in the counts of non-DAs. For the total sample (blue line in Figure 10) the observed ratio at 12 500 K can be explained if 11±1 per cent of DAs turn into non-DAs, while for our volume corrected sample (orange line in Figure 10) the value is 14±3 per cent. Also, the envelope models employed Rolland et al. (2018) show that helium-rich DAs could turn into DCs by convective mixing when their effective temperature goes below 12 000, K. In Figure 5 we can see a nearly constant number of DAs between 14 000 K and 12 000 K, being a further possible evidence of objects transitioning from DAs to DBs due the convective mixing. It is also important to notice that spectroscopic WD catalogues report approximately 150 DBAs, objects with spectra showing both hydrogen and helium lines, concentrated around 13 000 K (Kepler et al. 2016b, 2015; Eisenstein et al. 2006; Kleinman et al. 2004), being another possible evidence of this transition due to the convective mixing.

Another hypothesis to explain the observed helium to hydrogen atmosphere WD number and density ratio behaviour is related to the different cooling times for different atmosphere compositions (Bergeron et al. 2001). Helium-rich atmosphere WDs are expected to cool faster since helium is less opaque than hydrogen. We calculated the ratio using the hydrogen-rich and helium-rich atmosphere WD fully evolutionary models from Romero et al. (2015) and found that the helium-rich evolutionary models would need to cool down at least three times faster than predicted until reaching 16 000 K to reproduce the observed ratio, which is unlikely.

Finally, we consider the possibility of multiple populations of WD stars, one of them with a higher probability of producing non-DAs. The nearly constant number of DAs between 14 000 K and 12 000 K could be explained by two populations, one only with objects older than 1 Gyr and the second with most younger objects than 0.75 Gyr. This scenario is not very probable, however, it still could reproduce the observed ratio.

6 CONCLUSIONS

We find that DAs and DBs show nearly the same mass distribution, both having a peak around $\sim$0.55 $M_\odot$. Also, the mass distributions have nearly the same shape between $\sim$0.45 $M_\odot$ and $\sim$0.95 $M_\odot$. However, the mass distribution for DAs shows an excess in the number of objects at higher and lower masses. This could be an indication of a population of DA WDs originating from interacting binaries. Also, we found that the DCs mass distribution has a peak at $\sim$0.7 $M_\odot$, which is $\sim$0.15 $M_\odot$ higher that the one observed in the DAs and DBs distributions.

Our calculations of the helium to hydrogen number ratio shows an increase from $\sim$0.075 to $\sim$ 0.36 at effective temperatures from 22 000 K to 12 000 K. The main hypothesis to explain this increase are: convective dilution and mixing, cooling rates with high dependence of the atmosphere composition and multiple population scenario.

Contrary to the results of Tremblay & Bergeron (2008), we do not find an increase of the helium to hydrogen number ratio for effective temperatures below 10 000 K. This is related to the fact that the sample considered in this work is significantly larger than that used by Tremblay & Bergeron (2008). Also, we extend the effective temperature range up to 30 000 K.

Our study indicates that the differences in the cooling for hydrogen-rich and helium-rich atmosphere WDs evolutionary models are not enough to explain the observed ratio. Also, to reproduce the ratio with multiple populations, we need at least two distinct population, where one of them has the total age smaller than 0.75 Gyr.

The most acceptable hypothesis to explain the increase of the helium to hydrogen atmosphere WD number ratio between 21 000 K and 15 000 K is the convective dilution of the hydrogen layers turning around 14±3 per cent of DAs into non-DAs. The increase from 15 000 K to 12 000 K is a consequence of the convective mixing(see Rolland et al. 2018). Also the estimated mass distribution for DCs indicates that non-DAs cooler than 10 000 K are on average $\sim$0.15 $M_\odot$ more massive than DAs in the same effective temperature range, which is expected since the more massive DAs have thin hydrogen layers, making the convective mixing and dilution more likely to occur (Romero et al. 2012).

ACKNOWLEDGEMENTS

We thank the referee for his suggestions and comments, that improved the paper.

GO, ADR, SOK and LAA received support from from CNPq and PRONEX-FAPERGS/CNPq (Brazil). DK received support from programme Science without Borders, MCIT/MEC-Brazil. This research has made use of NASA Astrophysics Data System.

Funding for SDSS-III has been provided by the Alfred P. Sloan Foundation, the Participating Institutions, the National Science Foundation, and the U.S. Department of Energy Office of Science. The SDSS-III web site is http://www.sdss3.org/.

SDSS-III is managed by the Astrophysical Research Consortium for the Participating Institutions of the SDSS-III Collaboration including the University of Arizona, the Brazilian Participation Group, Brookhaven National Laboratory, Carnegie Mellon University, University of Florida, the French Participation Group, the German Participation Group, Harvard University, the Instituto de Astrofísica de Canarias, the Michigan State/Notre Dame/JINA Participation Group, Johns Hopkins University, Lawrence Berkeley National Laboratory, Max Planck Institute for Astrophysics, Max Planck Institute for Extraterrestrial Physics, New Mexico State University, New York University, Ohio State University, Pennsylvania State University, University of Portsmouth, Princeton University, the Spanish Participation Group, University of Tokyo, University of Utah, Vanderbilt University, University of Virginia, University of Washington, and Yale University.

This work has made use of data from the European Space Agency (ESA) mission *Gaia* (`https://www.cosmos.esa.int/gaia`), processed by the *Gaia* Data Processing and Analysis Consortium (DPAC, `https://www.cosmos.esa.int/web/gaia/dpac/consortium`). Funding for the DPAC has been provided by national institutions, in particular the institutions participating in the *Gaia* Multilateral Agreement.

GO thanks Anna and her cat, Cosmos, for the company and support on this work.

REFERENCES

Abolfathi B., et al., 2017, preprint, (arXiv:1707.09322)
Althaus L. G., Córsico A. H., Isern J., García-Berro E., 2010, A&ARv, 18, 471
Bergeron P., Ruiz M. T., Leggett S. K., 1997, ApJS, 108, 339
Bergeron P., Leggett S. K., Ruiz M. T., 2001, ApJS, 133, 413
Bono G., Salaris M., Gilmozzi R., 2013, A&A, 549, A102
Brassard P., Fontaine G., Dufour P., Bergeron P., 2007, in Napiwotzki R., Burleigh M. R., eds, Astronomical Society of the Pacific Conference Series Vol. 372, 15th European Workshop on White Dwarfs. p. 19
Campos F., et al., 2016, MNRAS, 456, 3729
Carrasco J. M., Catalán S., Jordi C., Tremblay P.-E., Napiwotzki R., Luri X., Robin A. C., Kowalski P. M., 2014, A&A, 565, A11
Castanheira B. G., Kepler S. O., 2009, in Guzik J. A., Bradley P. A., eds, American Institute of Physics Conference Series Vol. 1170, American Institute of Physics Conference Series. pp 616–620, doi:10.1063/1.3246572
Doherty C. L., Gil-Pons P., Siess L., Lattanzio J. C., Lau H. H. B., 2015, MNRAS, 446, 2599
Doi M., et al., 2010, AJ, 139, 1628
Dufour P., Bergeron P., Fontaine G., 2005, in Koester D., Moehler S., eds, Astronomical Society of the Pacific Conference Series Vol. 334, 14th European Workshop on White Dwarfs. p. 197 (arXiv:astro-ph/0503448)
Eisenstein D. J., et al., 2006, ApJS, 167, 40
Fontaine G., Brassard P., 2008, PASP, 120, 1043
Gänsicke B. T., Koester D., Girven J., Marsh T. R., Steeghs D., 2010, Science, 327, 188
Garcia-Berro E., Hernanz M., Mochkovitch R., Isern J., 1988a, A&A, 193, 141
Garcia-Berro E., Hernanz M., Isern J., Mochkovitch R., 1988b, Nature, 333, 642
Gentile Fusillo N. P., Gänsicke B. T., Farihi J., Koester D., Schreiber M. R., Pala A. F., 2017, MNRAS, 468, 971
Green R. F., 1980, ApJ, 238, 685
Gunn J. E., et al., 1998, AJ, 116, 3040
Hamada T., Salpeter E. E., 1961, ApJ, 134, 683
Hansen B. M. S., et al., 2002, ApJ, 574, L155
Hansen B. M. S., et al., 2007, ApJ, 671, 380
Holberg J. B., Oswalt T. D., Sion E. M., McCook G. P., 2016, MNRAS, 462, 2295
Ibeling D., Heger A., 2013, ApJ, 765, L43
Isern J., García-Berro E., Salaris M., 2001, in von Hippel T., Simpson C., Manset N., eds, Astronomical Society of the Pacific Conference Series Vol. 245, Astrophysical Ages and Times Scales. p. 328
Kalirai J. S., Ventura P., Richer H. B., Fahlman G. G., Durrell P. R., D'Antona F., Marconi G., 2001, AJ, 122, 3239
Kalirai J. S., et al., 2013, ApJ, 763, 110
Kepler S. O., Kleinman S. J., Nitta A., Koester D., Castanheira B. G., Giovannini O., Costa A. F. M., Althaus L., 2007, MNRAS, 375, 1315
Kepler S. O., et al., 2015, MNRAS, 446, 4078
Kepler S. O., Koester D., Ourique G., 2016a, Science, 352, 67
Kepler S. O., et al., 2016b, MNRAS, 455, 3413
Kepler S. O., Koester D., Romero A. D., Ourique G., Pelisoli I., 2017, in Tremblay P.-E., Gaensicke B., Marsh T., eds, Astronomical Society of the Pacific Conference Series Vol. 509, 20th European White Dwarf Workshop. p. 421 (arXiv:1610.00371)
Kleinman S. J., et al., 2004, ApJ, 607, 426
Kleinman S. J., et al., 2013, ApJS, 204, 5
Koester D., 1978, A&A, 64, 289
Koester D., 2010, Mem. Soc. Astron. Italiana, 81, 921
Koester D., Kepler S. O., 2015, A&A, 583, A86
Koester D., Weidemann V., Zeidler E.-M., 1982, A&A, 116, 147
Koester D., Girven J., Gänsicke B. T., Dufour P., 2011, A&A, 530, A114
Liebert J., Bergeron P., Holberg J. B., 2003, AJ, 125, 348
Liebert J., Bergeron P., Holberg J. B., 2005, ApJS, 156, 47
Limoges M.-M., Bergeron P., 2010, ApJ, 714, 1037
Luri X., et al., 2018, preprint, (arXiv:1804.09376)
MacDonald J., Hernanz M., Jose J., 1998, MNRAS, 296, 523
Munn J. A., et al., 2014, AJ, 148, 132
Munn J. A., et al., 2017, AJ, 153, 10
Oswalt J. B. H. T. D., Sion E. M., McCook G. P., 2016, preprint, (arXiv:1606.01236)
Paczyński B., 1971, Acta Astron., 21, 417
Pelletier C., Fontaine G., Wesemael F., Michaud G., Wegner G., 1986, ApJ, 307, 242
Provencal J. L., Shipman H. L., Høg E., Thejll P., 1998, ApJ, 494, 759
Rebassa-Mansergas A., Nebot Gómez-Morán A., Schreiber M. R., Girven J., Gänsicke B. T., 2011, MNRAS, 413, 1121
Rebassa-Mansergas A., Rybicka M., Liu X.-W., Han Z., García-Berro E., 2015, MNRAS, 452, 1637
Renedo I., Althaus L. G., Miller Bertolami M. M., Romero A. D., Córsico A. H., Rohrmann R. D., García-Berro E., 2010, ApJ, 717, 183
Rolland B., Bergeron P., Fontaine G., 2018, ApJ, 857, 56
Romero A. D., Córsico A. H., Althaus L. G., Kepler S. O., Castanheira B. G., Miller Bertolami M. M., 2012, MNRAS, 420, 1462
Romero A. D., Campos F., Kepler S. O., 2015, MNRAS, 450, 3708
Schlegel D. J., Finkbeiner D. P., Davis M., 1998, ApJ, 500, 525
Schmidt M., 1968, ApJ, 151, 393
Schmidt M., 1975, ApJ, 202, 22
Sion E. M., Greenstein J. L., Landstreet J. D., Liebert J., Shipman H. L., Wegner G. A., 1983, ApJ, 269, 253
Stobie R. S., Ishida K., Peacock J. A., 1989, MNRAS, 238, 709
Torres S., García-Berro E., Burkert A., Isern J., 2002, MNRAS, 336, 971
Tremblay P.-E., Bergeron P., 2008, ApJ, 672, 1144
Tremblay P.-E., et al., 2017, MNRAS, 465, 2849
Winget D. E., Kepler S. O., 2008, ARA&A, 46, 157
Winget D. E., Hansen C. J., Liebert J., van Horn H. M., Fontaine G., Nather R. E., Kepler S. O., Lamb D. Q., 1987, ApJ, 315, L77
Woosley S. E., Heger A., 2015, ApJ, 810, 34
Yuan H. B., Liu X. W., Xiang M. S., 2013, MNRAS, 430, 2188
Yungelson L. R., 2008, Astronomy Letters, 34, 620

This paper has been typeset from a TEX/LATEX file prepared by the author.